Naval Research Laboratory
Stennis Space Center, MS 39529-5004

NRL/FR/7322--94-9601

Study of the Response of a Three-Dimensional Coupled Ice-Ocean Model to Daily Varying Atmospheric Forcing

SHELLEY K. RIEDLINGER
RUTH H. PRELLER

Ocean Dynamics and Prediction Branch
Oceanography Division

October 28, 1994

REPORT DOCUMENTATION PAGE

Form Approved OBM No. 0704-0188

1. AGENCY USE ONLY *(Leave blank)*	2. REPORT DATE	3. REPORT TYPE AND DATES COVERED
	October 28, 1994	Final

4. TITLE AND SUBTITLE

Study of the Response of a Three-Dimensional Coupled Ice-Ocean Model to Daily Varying Atmospheric Forcing

5. FUNDING NUMBERS

Job Order No.	573509304
Program Element No.	0603207N
Project No.	X0513
Task No.	100
Accession No.	DN894428

6. AUTHOR(S)

S. K. Riedlinger and R. H. Preller

7. PERFORMING ORGANIZATION NAME(S) AND ADDRESS(ES)

Naval Research Laboratory
Oceanography Division
Stennis Space Center, MS 39529-5004

8. PERFORMING ORGANIZATION REPORT NUMBER

NRL/FR/7322--94-9601

9. SPONSORING/MONITORING AGENCY NAME(S) AND ADDRESS(ES)

Commander, Space and Naval Warfare Systems Command
Code PMW 165-32
Washington, D.C. 22202

10. SPONSORING/MONITORING AGENCY REPORT NUMBER

11. SUPPLEMENTARY NOTES

12a. DISTRIBUTION/AVAILABILITY STATEMENT

Approved for public release; distribution unlimited.

12b. DISTRIBUTION CODE

13. ABSTRACT *(Maximum 200 words)*

The Naval Research Laboratory developed a coupled ice-ocean model that simulates ice-ocean interactions in response to atmospheric forcing. This model couples the U.S. Navy's Polar Ice Prediction System ice model, which is based on the Hibler ice model, to a diagnostic version of the Bryan-Cox three-dimensional ocean circulation model. A 6-yr simulation was performed using daily atmospheric data from the Fleet Numerical Meteorology and Oceanography Center's Naval Operational Global Atmospheric Prediction System (NOGAPS) for the years 1986 through 1991. Interannual variability in most NOGAPS fields was large. Ice thickness and ice concentration changes responded directly to fluctuations in surface forcing fields. The thinnest ice of the simulation occurred in 1989, 1990, and 1991. In 1990 and 1991, the surface air temperatures were warm compared to the other years, but in 1989 the net longwave radiation from NOGAPS was anomalously large in the summer. In the summer, solar and sensible heat fluxes are the strongest forcing fields, and they add heat into the ice-ocean system causing ice to melt. In the fall, solar heating diminished and the combination of sensible plus latent fluxes, along with longwave radiation, caused a dramatic cooling that resulted in ice growth. In the winter, the sensible heat flux added heat into the system, but the combination of latent heat flux and longwave cooling dominated; the result was further ice growth. Winds have a pronounced effect on ice growth/melt by directly altering the sensible and latent heat fluxes and by indirectly affecting all heat fluxes by altering the distribution of ice cover and open water. Ice advection may account for more than half of the change in ice thickness in any given month when the winds are strong. Ocean temperature and salinity also showed interannual and seasonal variability in response to atmospheric forcing. Sensitivity studies were performed using atmospheric climatology, similar to that used in previous ice-ocean model studies, versus the daily NOGAPS forcing. Due to a simplistic representation for cloud cover and the omission of the diurnal cycle, the climatological solar fluxes were large compared to the NOGAPS values, which resulted in thinner ice cover in these model simulations. Additional sensitivity studies are presented that (1) replaced the climatological solar fluxes and (2) replaced the climatological winds with NOGAPS.

14. SUBJECT TERMS

sea-ice forecasting, sea-ice models, sea-ice analysis

15. NUMBER OF PAGES

29

16. PRICE CODE

17. SECURITY CLASSIFICATION OF REPORT	18. SECURITY CLASSIFICATION OF THIS PAGE	19. SECURITY CLASSIFICATION OF ABSTRACT	20. LIMITATION OF ABSTRACT
Unclassified	Unclassified	Unclassified	Same as report

UNCLASSIFIED

CONTENTS

STUDY OF THE RESPONSE OF A THREE-DIMENSIONAL COUPLED ICE-OCEAN MODEL TO DAILY VARYING ATMOSPHERIC FORCING

1.0 INTRODUCTION

A sea-ice forecast model, the Polar Ice Prediction System (PIPS) (Preller and Posey 1989), is run operationally at the Fleet Numerical Meteorology and Oceanography Center (FNMOC). This model is driven by daily forecasts of atmospheric forcing from the Navy Operational Global Atmospheric Prediction System (NOGAPS) model. Oceanic forcing is supplied by monthly mean geostrophic ocean currents and monthly mean oceanic heat fluxes derived from the Hibler and Bryan (1987) coupled ice-ocean model. Recent improvements by the Naval Research Laboratory (NRL) to this forecast model were directed toward developing a coupled ice-ocean forecast model similar to that of Hibler and Bryan. Previous NRL studies with this coupled model (Riedlinger and Preller 1991) showed improvement in the capability of forecasting the advance and retreat of the ice edge.

Atmospheric heat fluxes and surface stresses are important to the formation and movement of ice. Inadequate forcing data, whether short-term (daily) errors or an accumulation of long-term biases, would degrade an ice model's forecasting capability. Thus, to better understand the effects of forcing on the coupled ice-ocean system, a 6-year simulation of the ice-ocean model was run using 6 consecutive years of forcing data from NOGAPS. The results from this simulation were studied to determine the effect of forcing on such fields as ice thickness, ice drift, ocean temperature, and salinity. Additional model runs driven by climatic representations of the fluxes were compared to the first simulations to help clarify the relative importance of these fluxes.

2.0 MODEL DESCRIPTION

The coupled ice-ocean dynamic/thermodynamic sea-ice model used is the result of coupling PIPS to the Bryan-Cox (Cox 1984) ocean circulation model. For a more detailed description of the coupled model, see Riedlinger and Preller (1991).

The PIPS ice model is based on the Hibler dynamic/thermodynamic sea-ice model. The ice model has five major components: a momentum balance, ice rheology, ice thickness and concentration distribution, ice strength, and an air-ice-ocean heat balance. The ice thickness distribution evolves as a result of dynamic and thermodynamic effects. The seven-level ice thickness calculations of Walsh et al. (1985) are incorporated into the ice model to better predict ice growth rates by increasing the dependence of ice growth rates on ice thickness. The thermodynamic portion of the ice model determines growth and decay rates of ice on the basis of a heat budget balance among the atmosphere, the ice, and the ocean, including the effects of heat absorbed by leads via lateral mixing. In the presence of an ice cover, the first ocean level is kept at the freezing point, which

is dependent on the salinity at this level. Thus, any heat input into the first level of the ocean model will reduce the vertical growth rate of ice. Heat absorbed by open-water areas can reduce the areal extent of ice via lateral melting. Heat absorbed by open water increases the temperature of level 1 and, to a lesser extent, the temperature of deeper levels. When cooling begins in the fall and ice starts to reform, heat stored in the ocean is released during convective mixing. This heat reduces the growth rate of ice, and delays ice accumulation until the mixed-layer temperature returns to the freezing point.

The dynamic portion of the ice model computes a momentum balance for ice drift using geostrophic winds, ocean currents from the first level of the ocean model, and an internal ice stress force. The viscous-plastic constitutive law described by Hibler (1979), which relates internal ice stress to ice deformation and ice strength, is used to determine the internal ice force.

The horizontal model grid (Fig. 1) is a subsection of an FNMOC standard polar stereographic grid of the northern hemisphere covering the Arctic basin, the Barents Sea, and the Greenland/ Norwegian Seas. The grid is defined to be equally spaced between the FNMOC standard gridpoints, resulting in a spacing of approximately 127 km in the x and y directions. The thermodynamic variables are defined at these points. The dynamic variables are defined one-half a grid distance from the thermodynamic variables.

Solid-wall boundary conditions are used at all boundaries in the ice model, except for the southern boundary across the Greenland/Iceland and Norwegian Seas, which is an ice outflow boundary. Ice can be transferred into these boundary grid cells only by advection and, once there, is removed from the basin.

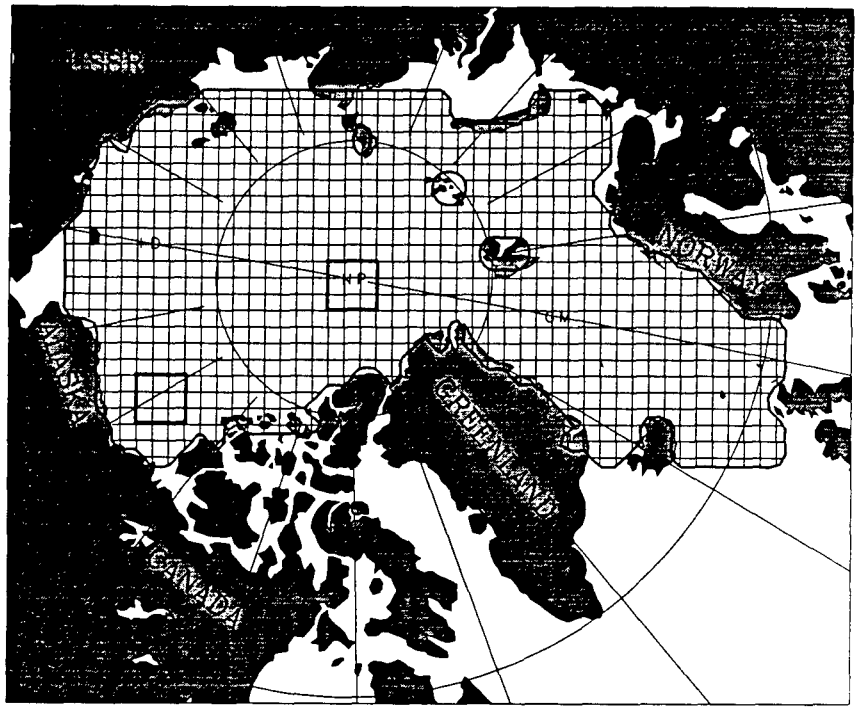

Fig. 1 — The 47 x 25 horizontal model grid. Boxes depict Beaufort Sea and central Arctic regions used in later discussions.

The ocean model is the Bryan-Cox (Cox 1984) three-dimensional, primitive equation, general circulation model that simulates large-scale features of baroclinic circulation. The lateral boundary conditions used define rigid walls at the outside gridpoints. These boundary conditions are implemented as in Sarmiento and Bryan (1982). The southern solid-wall boundary of the ocean model is set just south of the Denmark Strait and the Iceland–Færoe–Shetland Channel. Since the horizontal grid spacing used does not resolve the circulation through the Bering Strait, a simple solid-wall boundary is applied.

Bottom topography for the Arctic was obtained from the Digital Bathymetric Data Base, Version 5 (DBDB5) data (Naval Oceanographic Office 1987). These data were interpolated to the model grid and then smoothed. The vertical grid consists of 15 levels from the surface to 5700 m deep with varying layer thicknesses. The thicknesses of the levels increase from 30 m at level 1 to a thickness of 1025.5 m at level 15. The temperature, salinity, and current values are defined at the midpoints of the levels, and the vertical velocity is defined at the interface of each level.

Levitus' (1982) winter climatological temperatures and salinity were used to initialize the ocean model. This climatology was also used to constrain the computed ocean temperature and salinity. A 3-year constraint was used on levels 2 and below, a 30-day constraint was used on the southern solid wall boundary and the Bering Strait, and no constraint was placed on level 1.

The ice model provides the surface boundary conditions of heat flux, salt flux, and surface stresses to the ocean model. The ocean model supplies the heat exchange at the ice-ocean interface and the ocean currents to the ice model. Stresses are defined using geostrophic winds and the ocean current from level 1 of the ocean model.

The oceanic heat flux F_W, the heat brought into level 1 by horizontal and vertical advection, diffusion, and convection, is used in the ice model's heat budget and is computed from

$$F_W = \Delta T \; C_c \; h_w / \Delta t \,, \tag{1}$$

where C_c is the volumetric heat capacity of seawater, h_w is the thickness of the first level in the ocean model, and Δt is the time step. The variable ΔT is the change in temperature in level 1 due to horizontal and vertical advection, diffusion and convection.

The salt flux S_f is computed from the change in ice thickness as

$$S_f = [\Delta h_i (S_w - S_i)] / (h_w \; \Delta t) \,, \tag{2}$$

where $\Delta h_i / \Delta t$ is the growth/melt rate of ice in meters per second. The quantity $(S_w - S_i)$ is the difference in the average salinity of seawater (35 ppt) and the salinity of ice (assumed to be 5 ppt). If no ice exists in a grid cell, then no salt flux is passed to the ocean model.

The temperature in the ocean is updated as

$$T^{n+1} = T_F{}^{n+1} + \Delta T + H_c \,, \tag{3}$$

where $T_F{}^{n+1}$ is the freezing temperature computed using the updated salinity S^{n+1}, and H_c is the heat stored in level 1 of the ocean. If ice exists in a grid cell, then the temperature of level 1 remains at the freezing temperature and H_c is zero. If the grid cell is ice-free, then H_c is increased or decreased according to the heat budget calculations in the ice model.

The salinity equation is

$$S^{n+1} = S^n + \Delta S + S_f \, \Delta t \,, \tag{4}$$

where S^n is the salinity at the present time step and ΔS is the change in salinity in level 1 of the ocean model. The temperature and salinity in the ocean model are convectively adjusted by averaging adjacent levels when the density of adjacent levels indicates a density instability.

3.0 ATMOSPHERIC FORCING FIELDS

The ice-ocean model was driven with atmospheric forcing data from the NOGAPS atmospheric model (Hogan et al. 1990; Hogan and Rosmond 1991). Data from 6 sequential years, 1986 through 1991, were used to force the model. The 6- or 12-hourly analysis fields from NOGAPS were linearly interpolated to the 2-hour time step used in the model. The forcing fields used were surface air pressure, vapor pressure, surface air temperature, solar radiation, total heat flux, and sensible plus latent heat flux (see Table 1).

Table 1 — NOGAPS Analysis Fields Used as Model Forcing

SURFACE AIR PRESSURE (mb): used to compute the geostrophic winds.
VAPOR PRESSURE (mb): used along with the surface air pressure to compute specific humidity, which in turn is used to compute the latent heat flux.
SURFACE AIR TEMPERATURE (°C): used to compute sensible heat.
SOLAR RADIATION (cal/cm^2/h): incoming shortwave radiation.
TOTAL HEAT FLUX (cal/cm^2/h): i.e., the sum of net longwave radiation, sensible heat, latent heat, and solar radiation used to compute the net longwave radiation.
SENSIBLE + LATENT HEAT FLUX (cal/cm^2/h): used with the solar radiation and total heat flux to compute the net longwave radiation.

The NOGAPS model has undergone several changes during these years (Table 2). In 1988, NOGAPS was changed to a spectral model (Hogan and Rosmond 1991). Several adjustments were made to the new atmospheric model. As a result, NOGAPS forcing for most of 1988 (January through August) was not used in the ice-ocean model simulations but was replaced with an average of the forcing data from 1986, 1987, and 1990. Some adjustments were still being made to the model in 1989. It was decided that these data would be used in the simulation but not in the average forcing.

Table 2 — History of NOGAPS from 1986–1990

July 1986, NOGAPS 2.2: corrected for deficiencies in ground temperatures and wetness (9-layer finite difference PE model 2.4° × 3.0° grid resolution).
January 1988, NOGAPS 3.0: first spectral model, 47 wave, 2.5° resolution, 18 levels.
March 1989, NOGAPS 3.1: corrections to radiative forcing.
August 1989, NOGAPS 3.2: high-resolution model, 79 wave, 1.5° resolution, 18 levels.

The surface air pressure was one field from NOGAPS that can readily be compared to observations and consistently compares favorably with these observations. The annual average of NOGAPS air pressures for the model domain are shown in Fig. 2 for 1986 through 1991. The annual average air pressure from buoy data compiled by Colony and Rigor (1989, 1991a–d) for 1986 through 1990 are shown in Fig. 3. Both figures show a pattern of high pressure in the western Arctic and relatively low pressure in the eastern Arctic. The annual trend in air flow is from the Russian coast across the Arctic basin to

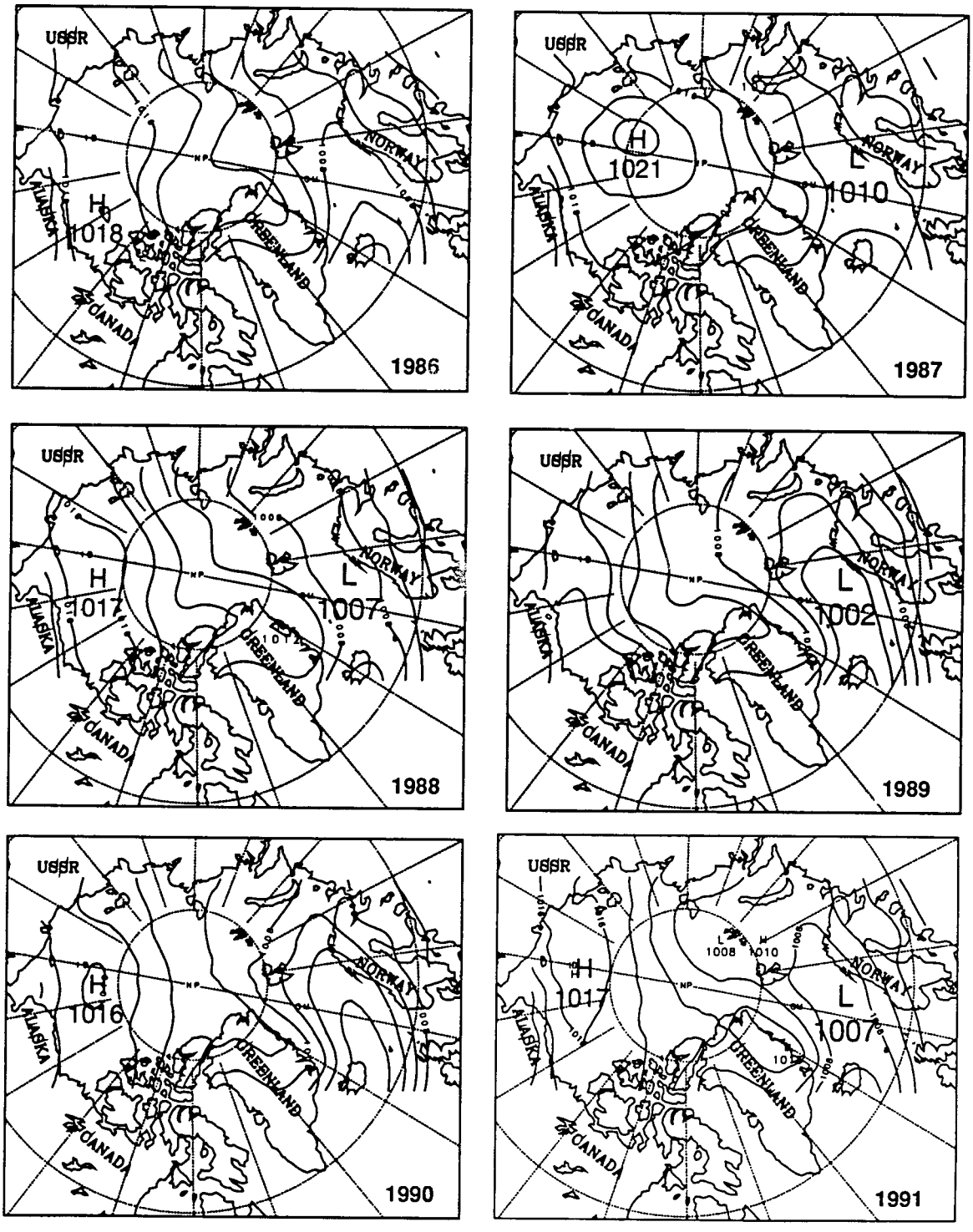

Fig. 2 — Annual mean air pressures from NOGAPS. Contour interval is 2 mb.

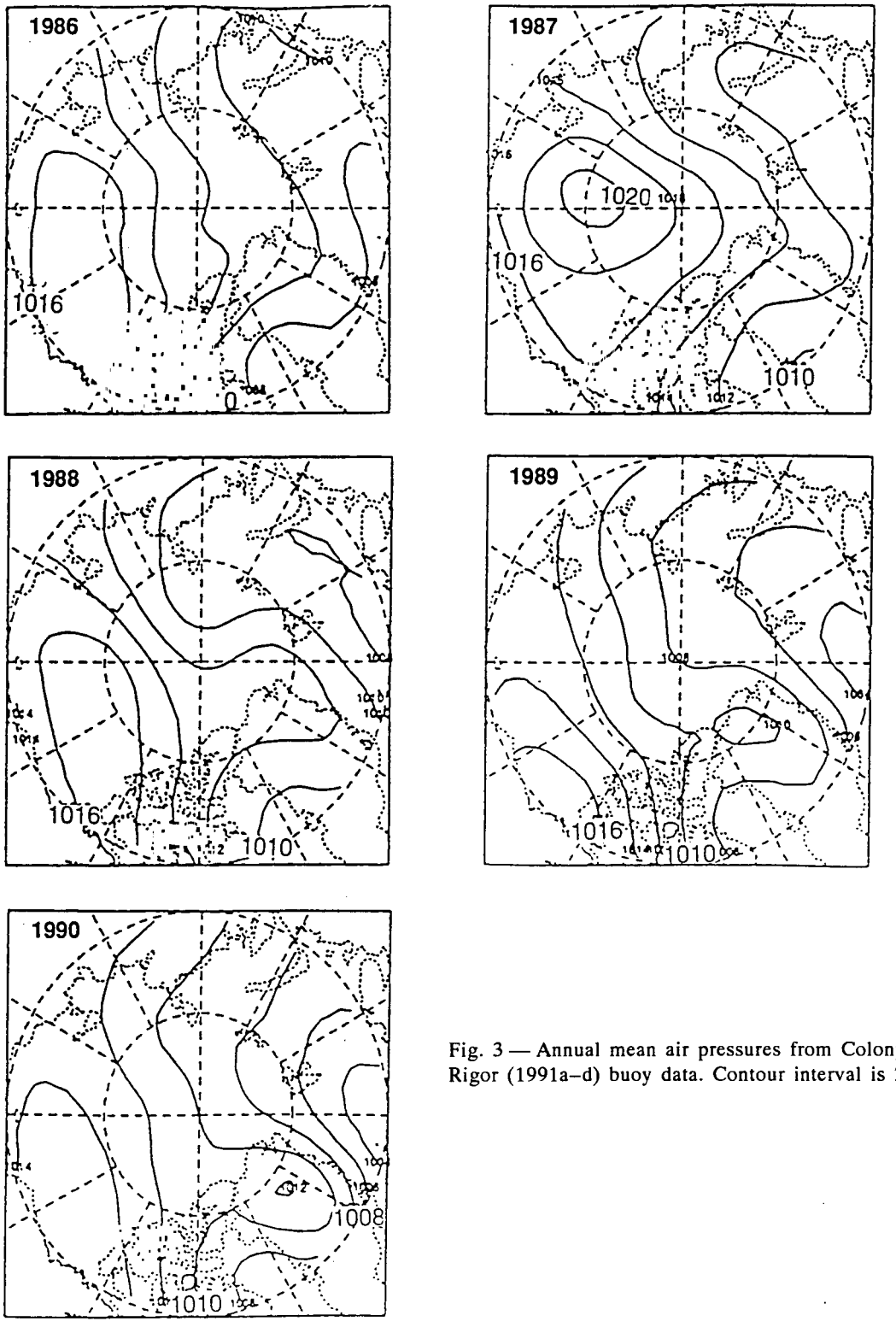

Fig. 3 — Annual mean air pressures from Colony and Rigor (1991a–d) buoy data. Contour interval is 2 mb.

the Canadian and Greenland coasts. In some years this flow is stronger and is more concentrated along the Canadian coast (e.g., in 1986); in other years, the flow is concentrated along the north Greenland coast (e.g., in 1987). Similarly, although winds normally flow from the North Pole through the Fram Strait (e.g., in 1989), during some years they came from north of the islands, Franz Josef Land, and Svalbard (e.g., in 1987). These changes in wind direction will affect the amount and the thickness of ice being transported through the Fram Strait.

The annual air temperature from NOGAPS (not shown) indicates that 1986 was the coldest of the 6 years along the Canadian coast and northward through the central Arctic. The years 1990 and 1991 were the warmest in this region. In the marginal seas, air temperature was 2° to 4° warmer off the east coast of Greenland in 1987 and 1988 (–10°C to –6°C) when compared to 1989 and 1990 (–14°C to –8°C). In the Barents Sea the warmest temperatures occurred in 1988 and 1990.

4.0 MODEL RESULTS

4.1 Interannual Variability

The ice-ocean model was spun-up for 6 years using the 1986 NOGAPS forcing. At the end of the spin-up, the model was run for an additional 6 years using the 1986 through 1991 forcing fields.

The annual average ice drift is shown in Fig. 4. Ice drift in many areas follows the pattern of the winds. Two such areas are along the Canadian coast and through the Fram Strait. In regions where the winds are weak, ocean currents can have a greater influence on ice drift. Annual ocean currents (level 1) for the sample year of 1987 are shown in Fig. 5. The general circulation features known to exist in the Arctic, e.g., the Beaufort gyre and transpolar drift, are observed in the model currents. The magnitude of the annual average oceanic flow is generally less than 30 cm/s. In many regions, the winds and the ocean currents are similar in direction.

The annual average ice thickness for each year of the simulation is shown in Fig. 6. The general distribution of ice thickness agrees with the observations of Bourke and Garrett (1987). The thickest ice occurs each year along the Canadian archipelago. Ice thickness thins toward the central Arctic and becomes very thin along the Eurasian coast.

Year-to-year variability is observed in the maximum ice thickness, the ice distribution along the Canadian and north Greenland coasts, and the position of the ice edge. Ice thickness in 1986 exceeded 6 m near Ellesmere Island. This was the thickest ice found in the simulation. Both the cold air temperatures and the wind-driven ice drift contributed to the build-up of ice in the region that year. In 1987, thick ice was concentrated in a smaller area along the archipelago, while in 1989, thick ice was spread out all along the archipelago and along the north coast of Greenland. Ice was relatively thin (<1.5 m) along the east coast of Greenland in 1987 and 1988. The thickest ice in the region occurred in 1989. These trends correspond to warmer air temperatures in this region in 1987 and 1988 and to colder air temperatures in 1989. Winds and the resulting ice drift appear to have aided the thin ice conditions in 1987 and the thick ice conditions in 1989. In 1987, ice passing through the Fram Strait is primarily thin ice from just north of Franz Josef Land and Svalbard. In 1989, thick ice from near the North Pole passes through the Fram Strait.

4.2 Time Series

Two subregions of the model domain, the Beaufort Sea and the central Arctic (Fig. 1), will be used to examine ice-ocean model response to seasonal and shorter time scale variability in the

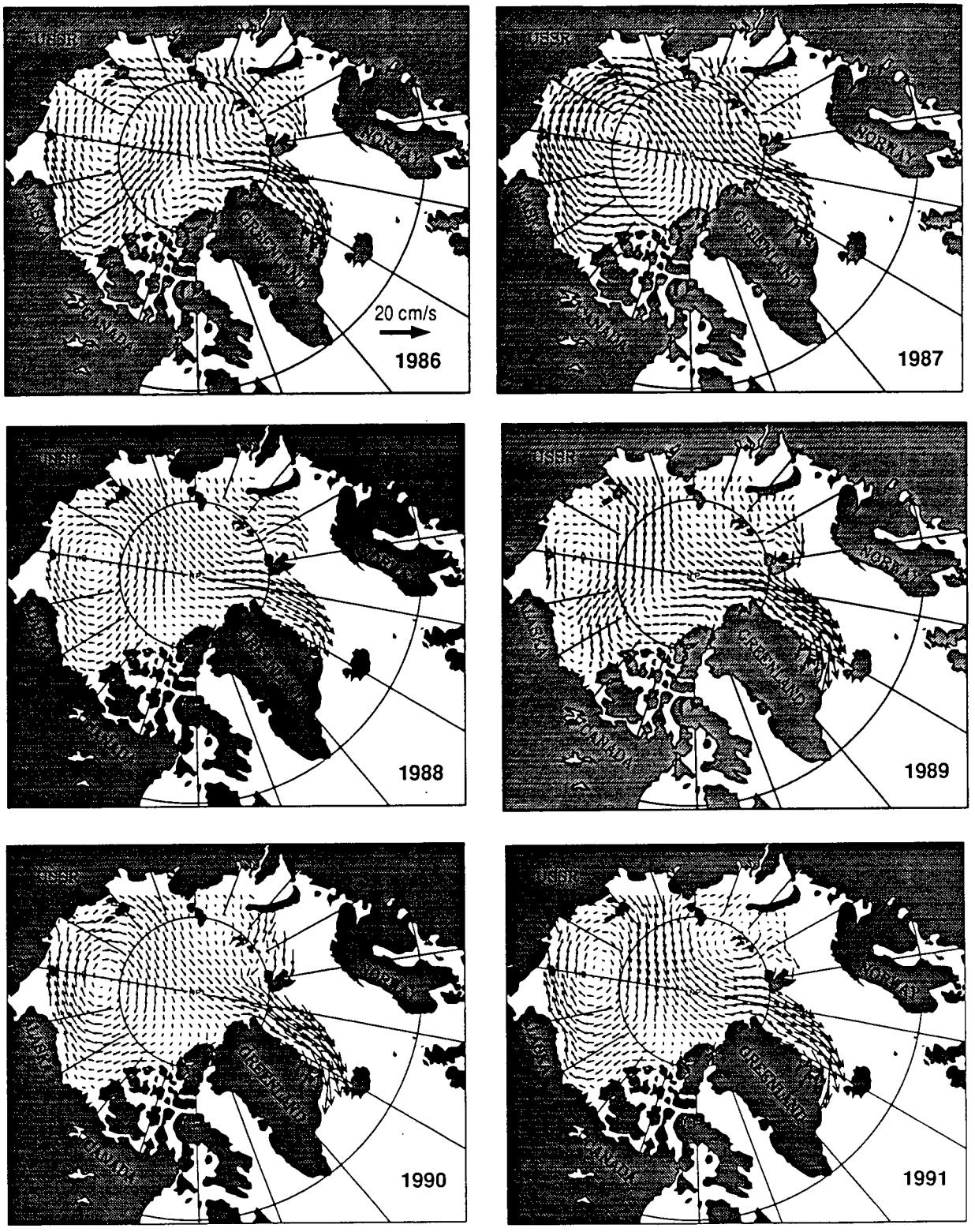

Fig. 4 — Annual mean model-derived ice drift. Maximum vector is 20 cm/s.

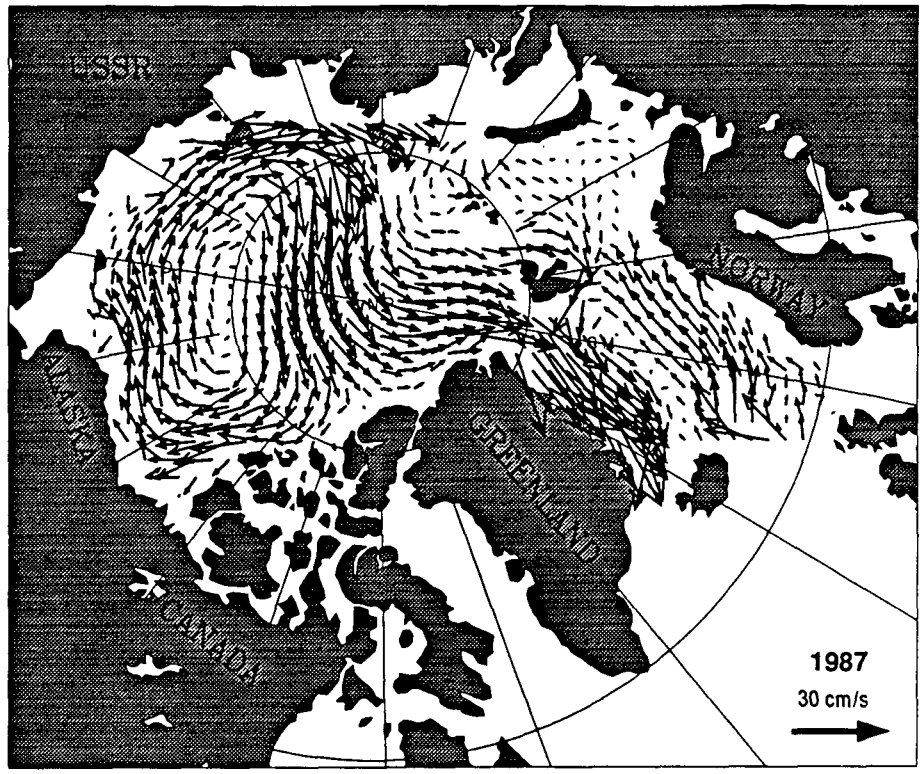

Fig. 5 — Annual mean model-derived ocean currents at level 1. Maximum vector is 30 cm/s.

forcing data. All discussions in this section will refer to areal averages formed by averaging atmospheric input and model output over the 16 gridpoints within each regional box (shown in Fig. 1). NOGAPS forcing data at 6-hour intervals from 1986 through 1991 are plotted in Fig. 7 (Beaufort area) and in Fig. 8 (central Arctic). The wind speeds for each area are shown in Fig. 9.

Air temperatures in the Beaufort (Fig. 7a) during the summers of 1990 and 1991 are warmer than in any of the other years, frequently reaching or exceeding 10°C. Monthly average air temperatures listed in Table 3 show that 1990 has the warmest air temperatures for 7 months out of the year, with 1991 being a close second. The coldest air temperatures occurred in January 1986 and February 1987. Late fall 1989 and winter 1990 are the only fall/winter periods in the Beaufort in which air temperatures were consistently cold (<–18°C). Warm periods often occur in the winter and/or fall of the other years. A strong midwinter warming occurs in February 1986 and in February 1989. Strong warming also occurs in December 1987 and December 1988.

The net longwave radiation (Fig. 7b, Table 4) is generally negative (implying cooling). The strongest cooling most often occurs in April, and occasional positive values occur in June and July. The most noticeable feature in the longwave data is the large positive anomaly in 1989. This anomaly probably reflects adjustments to the NOGAPS model as opposed to a real trend in the atmosphere. In August 1989, NOGAPS was updated with higher resolution (Table 2). After this update, no similar irregularities have appeared in the NOGAPS forcing data in the Arctic. The solar radiation (Fig. 7c) is the strongest in the summer of 1987 and the weakest in the summers of 1990 and 1991. The specific humidity (Fig. 7d), generally near zero in the winter and at its maximum in the summer, reflects many of the same trends and fluctuations observed in the air temperature. The largest specific humidity values occur in the summer of 1990. Significant increases in the

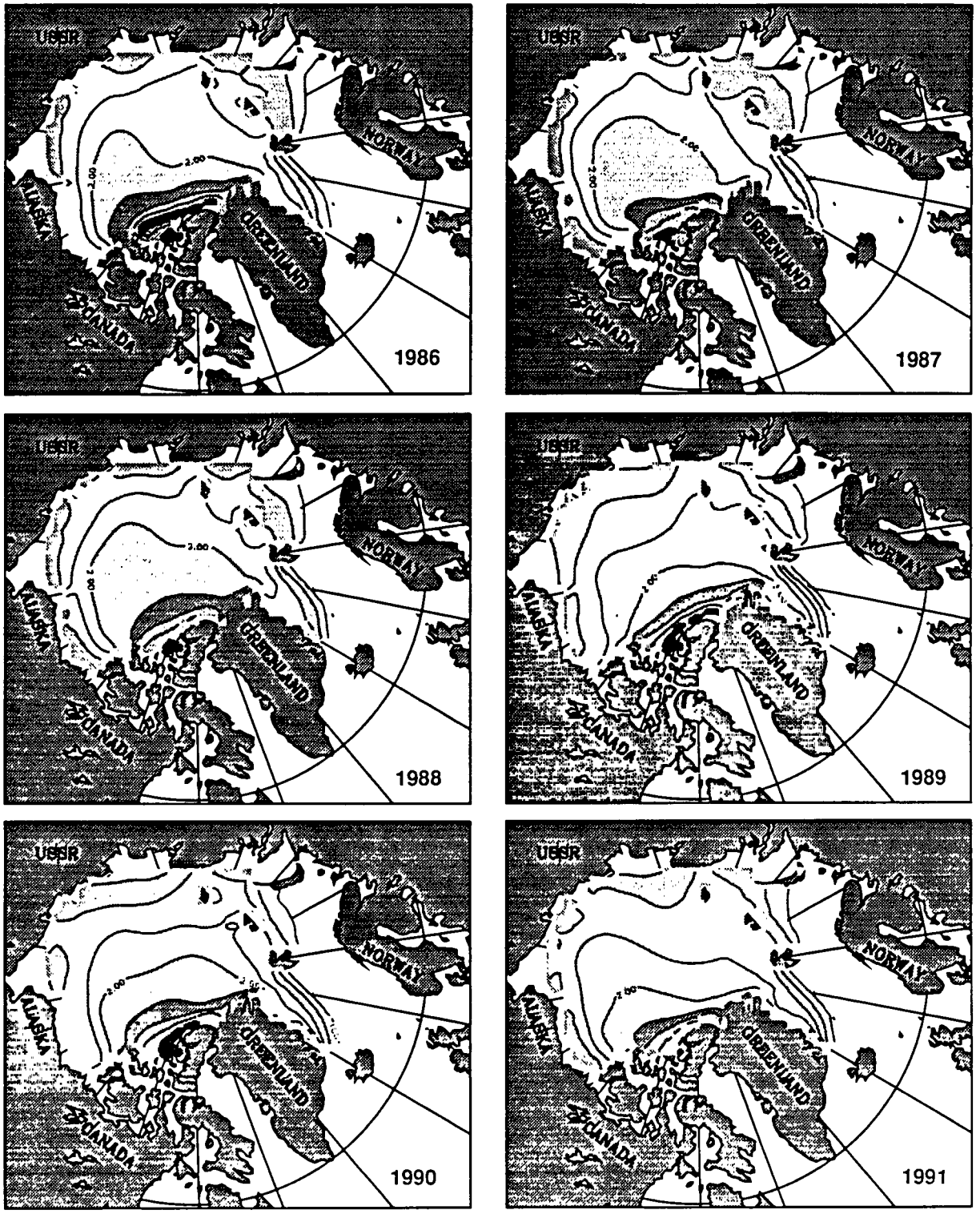

Fig. 6 — Annual mean model derived ice thickness. Ice edge is denoted by the 0.1-m contour. Contour interval is 0.5 m for other contours.

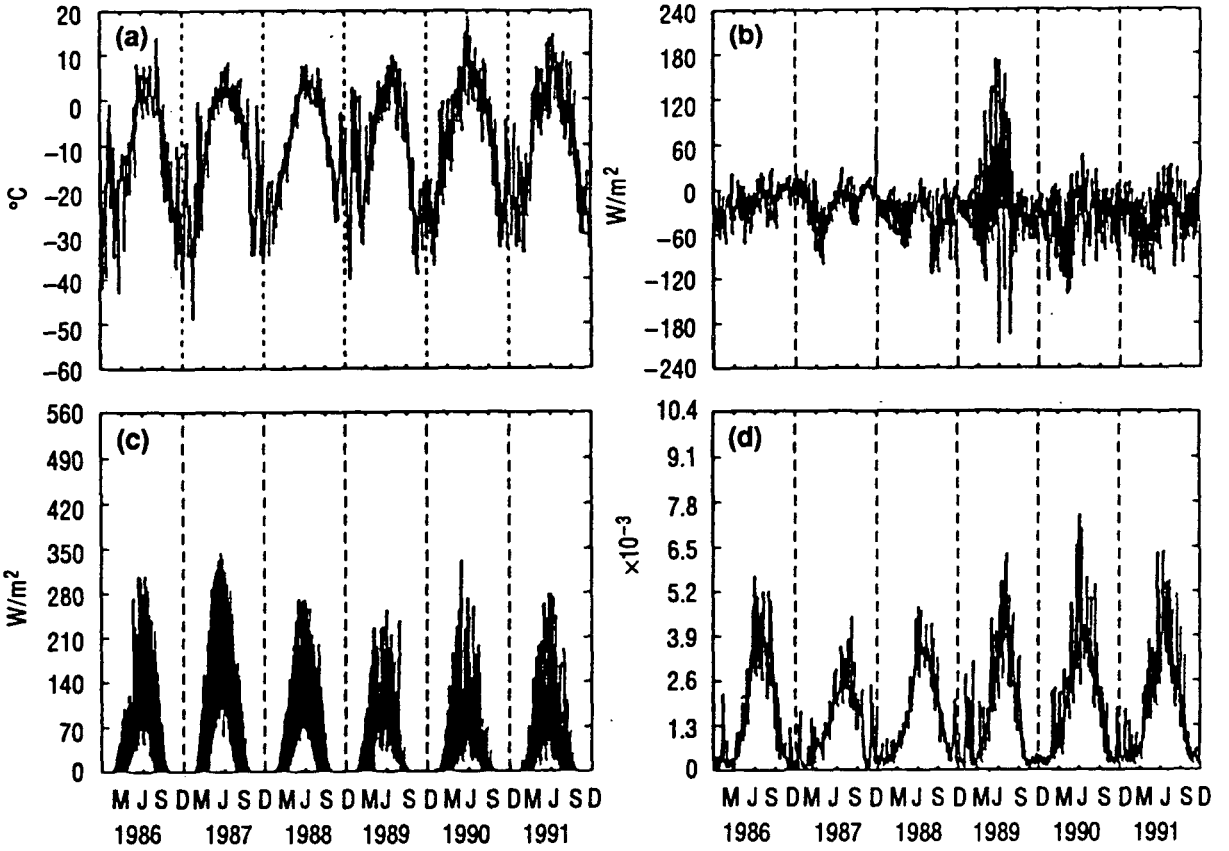

Fig. 7 — Areal-averaged input fields from NOGAPS at 6-hour intervals. All data are for the Beaufort region. (a) Air temperature, (b) longwave radiation, (c) solar radiation, and (d) specific humidity.

specific humidity occur in February 1986 and 1989, as well as in December 1987 and 1988. The increases correspond to warming events in the air temperature.

In the central Arctic (Fig. 8) surface air temperatures were coldest in the winter of 1986, while the warmest summer occurred in 1991. Warm periods observed in the winter and fall in the Beaufort also occurred in the central Arctic, although not always at the same time. The maximum solar fluxes occurred in 1987 in the central Arctic just as in the Beaufort. The anomalous positive net longwave values in 1989 were also seen in the central Arctic but were greatly reduced in magnitude. Large positive values of net longwave radiation data were observed in other Arctic regions, so this trend in 1989 was widespread in NOGAPS. The specific humidity in the central Arctic, as in the Beaufort, followed the trends and the fluctuations in the air temperature.

The wind speeds (Fig. 9) were highly variable in both the Beaufort and the central Arctic. In 1988, wind speed decreased as expected, since this was an average of 1986, 1987, and 1990. Wind speeds are generally stronger in the fall and winter and are weaker in the summer. The decrease in speed in the summer was much less in the central Arctic. The magnitude of the average wind speed was usually larger in the central Arctic than in the Beaufort.

The model-generated ice thickness for the Beaufort and central Arctic are shown in Fig. 10. Some of the ice thickness trends appear to follow trends in the air temperature. For example, the warm periods in February of several years correspond to either a slower ice thickness increase or

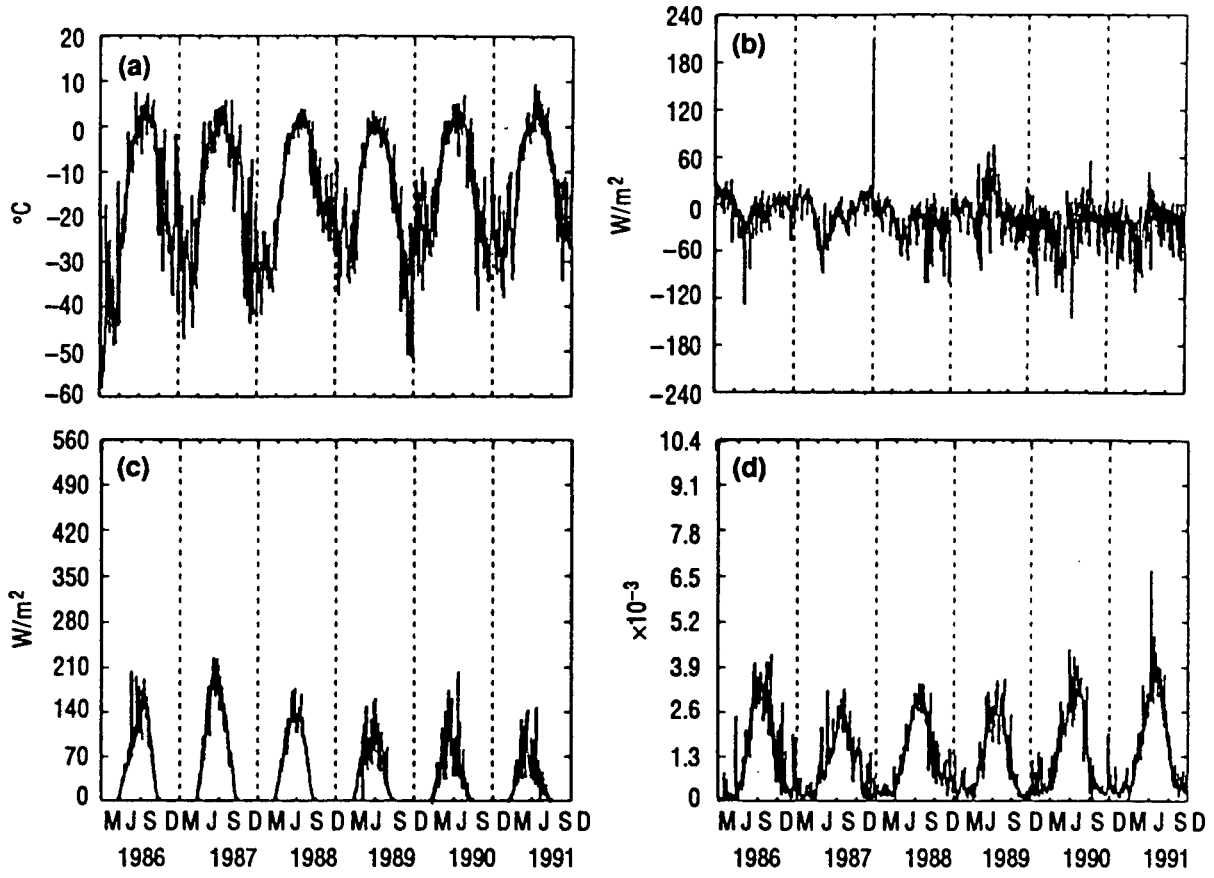

Fig. 8 — Areal-averaged input fields from NOGAPS at 6-hour intervals. All data are for the central Arctic region. (a) Air temperature, (b) longwave radiation, (c) solar radiation, and (d) specific humidity.

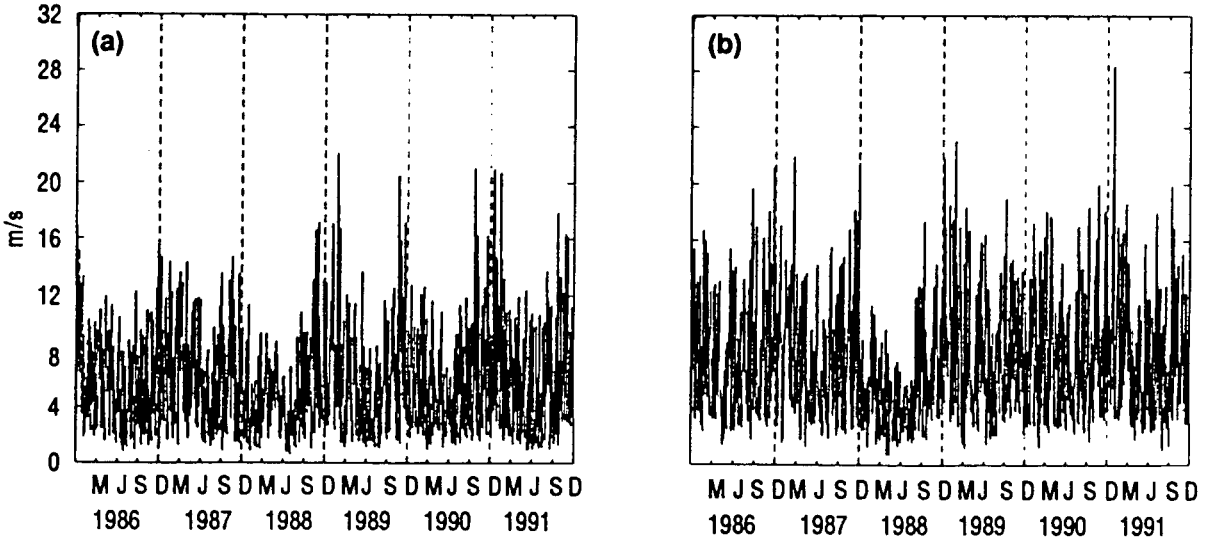

Fig. 9 — Areal-averaged wind speeds from NOGAPS at 6-hour intervals for (a) Beaufort region and (b) central Arctic region

Table 3 — Monthly Average Air Temperature and Solar Radiation from NOGAPS for the Beaufort Region

	1986	1987	1988	1989	1990	1991
Temperature (°C)						
Jan	−30.93	−24.35	−26.74	−24.86	−24.95	−20.60
Feb	−13.59	−31.26	−23.51	−6.72	−25.66	−23.71
Mar	−24.44	−19.53	−19.47	−20.98	−14.44	−21.69
Apr	−18.38	−12.62	−13.10	−14.52	−8.29	−9.11
May	−12.12	−2.85	−5.13	−5.96	−0.43	0.31
Jun	−1.26	0.45	1.21	−0.01	4.42	1.95
Jul	0.89	2.32	3.66	2.26	7.77	3.93
Aug	1.23	0.28	1.94	−1.90	4.31	2.86
Sep	0.68	−2.08	0.30	−1.90	0.78	−1.92
Oct	−12.37	−7.86	−8.39	−11.50	−7.94	−7.95
Nov	−21.98	−29.50	−17.86	−28.00	−20.02	−20.63
Dec	−25.09	−17.64	−14.18	−25.45	−22.40	−23.23
Solar Radiation (W/m^2)						
Jan	0.00	0.00	0.00	0.01	0.00	0.00
Feb	1.23	2.49	1.52	1.59	0.84	1.00
Mar	20.48	38.07	23.75	22.73	12.69	11.83
Apr	46.48	79.95	57.97	54.43	47.47	49.73
May	77.62	168.81	113.82	96.42	95.04	89.29
Jun	136.65	200.89	148.04	112.04	106.59	114.74
Jul	151.54	174.38	138.23	112.34	88.79	97.55
Aug	107.22	103.66	92.45	69.02	66.46	53.02
Sep	54.29	58.05	50.57	15.13	19.39	30.26
Oct	10.35	8.60	11.58	0.61	2.88	4.19
Nov	0.00	0.00	0.00	0.00	0.02	0.00
Dec	0.00	0.00	0.00	0.00	0.00	0.00

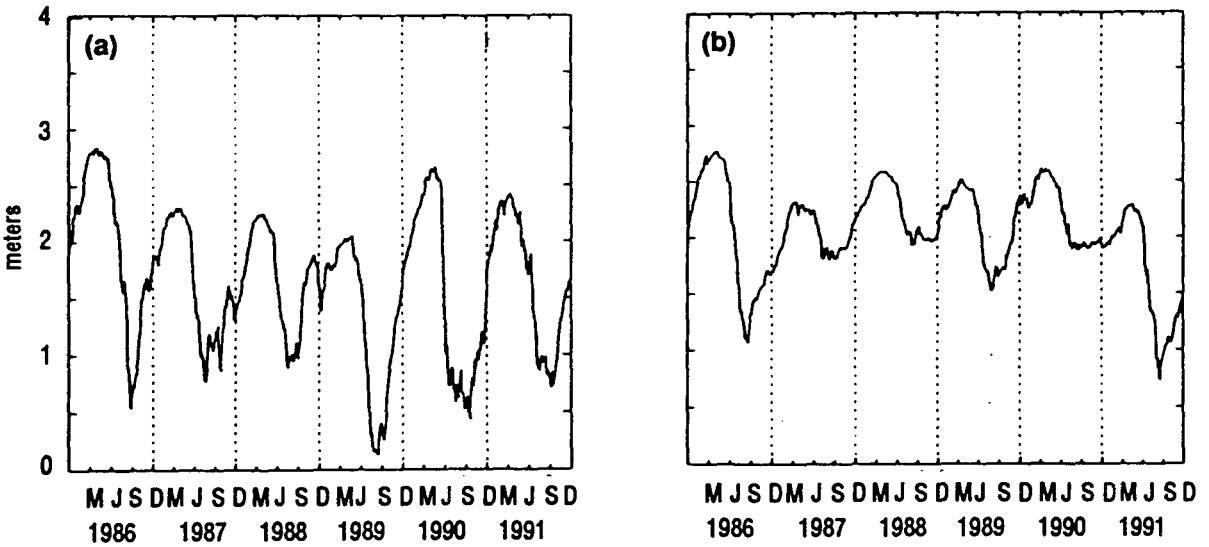

Fig. 10 — Model output areal-averaged ice thickness (meters) for (a) Beaufort and (b) central Arctic

Table 4 — Monthly Average of Net Longwave Radiation and Specific Humidity from NOGAPS for the Beaufort Region

	1986	1987	1988	1989	1990	1991
	Net Longwave Radiation (W/m^2)					
Jan	−32.67	1.75	−22.63	−22.67	−36.98	−32.25
Feb	−35.97	−3.30	−26.62	−26.69	−40.60	−35.42
Mar	−18.86	−22.85	−27.20	−26.18	−39.90	−41.51
Apr	−18.26	−39.01	−37.55	−34.02	−55.38	−54.81
May	−19.01	−45.16	−41.45	−24.04	−60.17	−53.21
Jun	−22.76	−26.36	−27.27	8.73	−32.68	−41.98
Jul	−13.25	−6.77	−10.66	15.23	−11.98	−18.33
Aug	−10.46	−7.22	−16.99	6.43	−33.29	−14.77
Sep	−5.20	−18.65	−64.73	−34.46	−24.57	−30.68
Oct	−10.27	−10.78	−47.95	−28.47	−32.36	−34.89
Nov	2.98	5.13	−36.95	−38.41	−27.99	−28.31
Dec	−0.13	1.63	−38.85	−41.36	−35.98	−27.48
	Specific Humidity ($\times 10^{-3}$)					
Jan	0.18	0.48	0.30	0.36	0.24	0.53
Feb	0.48	0.21	0.32	1.28	0.25	0.43
Mar	0.21	0.42	0.47	0.56	0.79	0.47
Apr	0.54	0.75	0.82	0.88	1.19	1.18
May	1.43	1.05	1.62	1.49	2.37	2.31
Jun	2.99	1.87	2.82	2.76	3.62	3.11
Jul	3.67	2.44	3.58	3.69	4.68	4.01
Aug	3.58	2.61	3.29	4.15	3.68	3.70
Sep	3.35	2.16	2.78	2.52	2.88	2.76
Oct	1.29	1.67	1.56	1.42	1.57	1.60
Nov	0.44	0.23	0.65	0.21	0.61	0.52
Dec	0.34	0.99	0.88	0.24	0.49	0.45

a decrease in ice thickness. In 1989, ice is kept thin by warm air temperatures in the winter and by large positive net longwave values in the summer. In 1989, solar fluxes are relatively small and do not contribute greatly to the decrease of ice thickness. The strong, consistent ice growth from October 1989 through March 1990 corresponds to consistently cold air temperatures during these months. Specific humidity and solar values are small during this period and net longwave is negative. All forcing fields encourage steady ice growth during this period.

The summer of 1990, the warmest of the 6 years of forcing studied, represents a period of strong ice melt. Specific humidity is also largest in 1990. Although the relatively weak solar flux and large net longwave radiation encourage thicker ice, the air temperature and specific humidity dominate, driving the strong summer ice melt. Strong melting also occurs in the summer of 1986. During this year the air temperature is not particularly warm when compared to 1990 or 1991, and the specific humidity is slightly smaller in magnitude than in 1990 and 1991. The solar flux, however, is relatively large and the net longwave flux is relatively weak, contributing to the strong melt in 1986.

Ice thickness variations from winter to summer are generally much smaller in the central Arctic (Fig. 10b) than in the Beaufort. Winter ice thickness is comparable in both regions; however, the summer melt is usually much less in the central Arctic. The greatest summer melt occurs in 1986, with ice melt in 1991 being a close second. Although the air temperatures are higher in the summer of 1991, the larger solar fluxes in 1986 compensate for the lower air temperatures and melt more ice than in 1991.

Many of the same fluctuations in ice thickness are observed in ice concentration (not shown). All years in both regions have 90 to 100% concentration in the winter. The summer of 1989 has the least concentration of ice in the Beaufort (minimum 25%) due to the thinner ice conditions in the winter and the large net longwave values in the summer. The maximum summer ice concentration occurs in 1988 and 1991 in the Beaufort region. These trends of maximum and minimum ice extent are not verified by the Navy/National Oceanic and Atmospheric Administration (NOAA) Joint Ice Center (1986–1991) ice concentration data and must be assumed to be due to changes in the NOGAPS model, as opposed to real physical changes in the atmosphere/ocean system.

The oceanic response to the atmospheric forcing and corresponding ice growth/melt is shown in Fig. 11 for the Beaufort region. The ocean temperatures (Fig. 11a) rise in the summer due to increased heating from warmer air temperature, increased solar fluxes, and increased percent of open water. The warmest ocean temperatures occur in the summer of 1989 and 1990. Both years experienced strong ice melt, resulting in thin ice and low ice concentrations. These thin ice conditions were attributed to large, positive, net longwave values in 1989 and to warm air temperatures in 1990. Ocean salinity plots (Fig. 11b) show lower salinities in the summer months due to ice melt

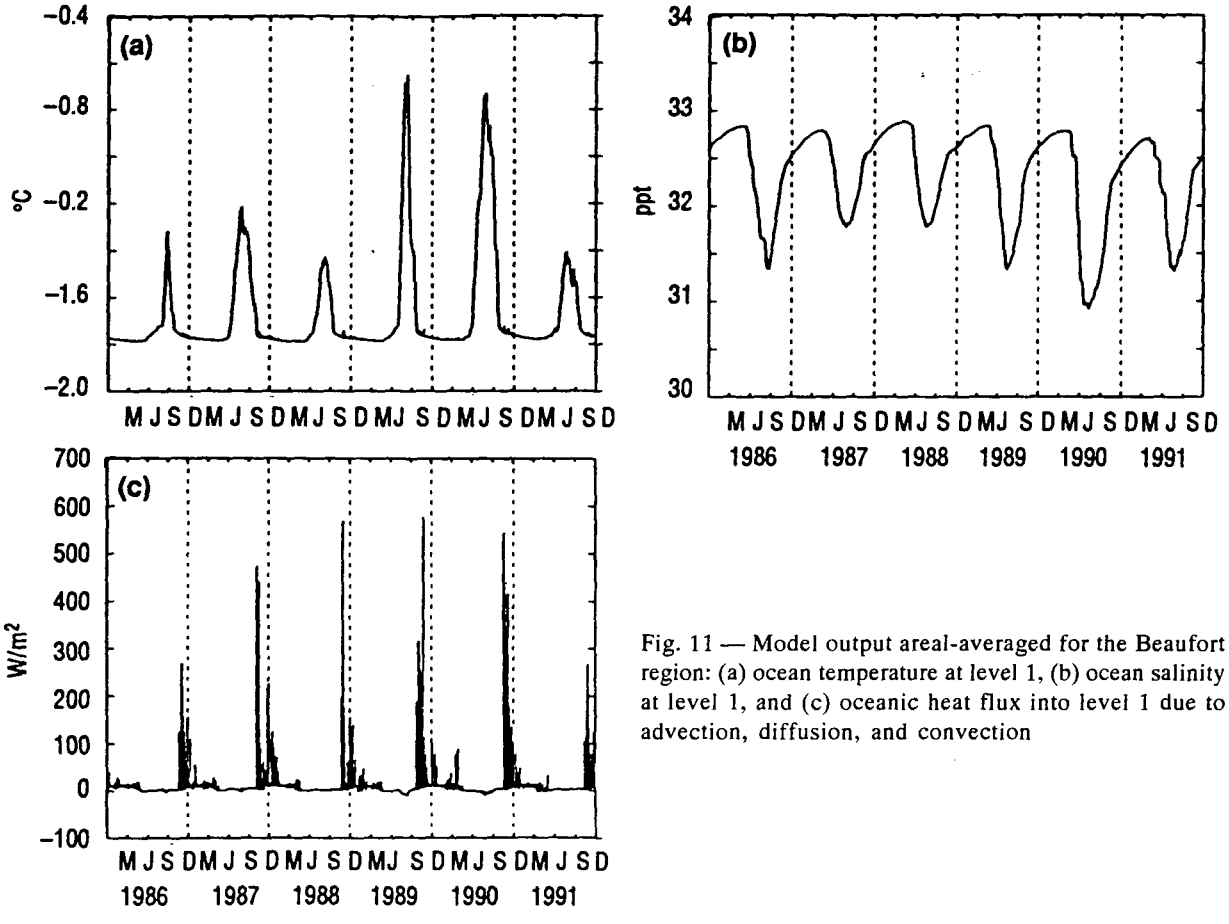

Fig. 11 — Model output areal-averaged for the Beaufort region: (a) ocean temperature at level 1, (b) ocean salinity at level 1, and (c) oceanic heat flux into level 1 due to advection, diffusion, and convection

and higher salinities in the fall due to ice growth. The lowest salinity value occurs in 1990 with relatively low salinities occurring in 1986, 1989, and 1991. These years also had very strong summer ice melt.

Oceanic heat flux F_W (Fig. 11c) is near zero in the summer. Ice melt shuts off convective mixing, the primary oceanic heating source of level 1. During the summer of 1989 and 1990 this quantity becomes negative, which indicates that heat from level 1 is being conducted downward into level 2. The warmest ocean temperatures occur during these years. Large, positive oceanic heat flux values occur in the fall of each year. These heat bursts correspond to ice formation and increased ocean salinities in level 1. The water column eventually becomes unstable due to increased density near the surface. Mixing with lower levels then takes place and causes the heat stored in the lower levels to be released. These bursts in oceanic heat flux either reduce ice growth or melt ice. Similar trends in the oceanic response occur in the central Arctic but have a much smaller amplitude.

From the discussion in this section, one sees the high degree of interannual and seasonal variability in the NOGAPS atmospheric forcing data. Also, the ice-ocean model responded directly to this forcing, both in ice growth/melt and in oceanic thermodynamics. Examining the forcing fields directly, however, did not lead to a well-defined consensus as to which fields dominate the ice growth/melt process. At times, one particular forcing field appeared to dominate; at others times all fields worked together to produce the same response; at still other times, forcing fields were similar in magnitude but were opposed to each other in their effect on ice growth/melt. In the following section, the atmospheric forcing fields will be used to compute net fluxes, weighted by the amount of ice cover. The sum of these heat fluxes at the air–ice–ocean interface (the net heat flux) will be related to the growth/decay of ice.

4.3 Net Forcing

Ice growth/decay is a result of the heat balance among the atmosphere, the ice, and the ocean. The incoming fluxes, as well as surface temperature and specific humidity discussed in the previous section, give some indication of how the ice and/or ocean will be affected by atmospheric forcing, but a more complete picture can be obtained by studying the net surface forcing. This means that the net heat balance at the surface of the ice or ocean is due to the incoming atmospheric fluxes and the outgoing oceanic fluxes. The flux balance must also be weighted by percent ice cover. The weighting is necessary, since each grid cell may contain some open water and since heat transfer between atmosphere and ocean and between atmosphere and ice occur at different rates. In this section, the net surface forcing will be examined and compared to ice growth/decay. The weighted heat fluxes—solar, sensible, latent and longwave—are computed as follows:

$$\text{solar: } (1-\alpha_{open})(1-A)F_S + (1-\alpha_{ice})A\ F_S \tag{5}$$

$$\text{sensible: } (1-A)F_{sen-open} + A\ F_{sen-ice} \tag{6}$$

$$\text{latent: } (1-A)F_{l-open} + A\ F_{l-ice} \tag{7}$$

$$\text{longwave: } F_L \tag{8}$$

F_S is the incoming solar flux, α is albedo ($\alpha_{open} = 0.1$ and $\alpha_{ice} = 0.65$), and A is percent of thick ice. $F_{sen-open}$ is the net sensible heat flux, assuming open water and no ice; $F_{sen-ice}$ is the net sensible heat flux, assuming ice cover and no open water; and F_{l-open} and F_{l-ice} are the latent heat flux for open water and ice cover, respectively. The net longwave term F_L is an input field from

NOGAPS and was shown in Fig. 7b. This term is not weighted since it is not possible to separate the incoming and outgoing parts of longwave radiation with the data available from NOGAPS.

The latent and sensible heat fluxes are computed from bulk heat transfer equations. Sensible heat is obtained from

$$F_{sen} = \rho_a \, c_p \, C_H |U_g| \, (T_a - T_s) \,, \tag{9}$$

where ρ_a is air pressure (assumed to be 1.3 kg m^{-3}), c_p is specific heat (1004 $Jkg^{-1}K^{-1}$), C_H is a transfer coefficient for sensible heat (1.75×10^{-3} for ice and 1.0×10^{-3} for open water), $|U_g|$ is the geostrophic wind speed, T_a is air temperature, and T_s is the temperature at the air/ice (if ice is present) or air/ocean (if no ice exists in a grid cell) interface. Latent heat is

$$F_1 = \rho_a \, L \, C_E \, |U_g| \, (q_a - q_s) \,, \tag{10}$$

where L is latent heat of vaporization (2.5×10^6 Jkg^{-1}) or sublimation (2.834×10^6 Jkg^{-1}), depending on the existence of ice or open water. C_E is a transfer coefficient for latent heat ($C_H = C_E$), and q_a and q_s are specific humidity for air at 10 m and at the ice/water surface, respectively.

This discussion concentrates on only the Beaufort Sea for 3 of the 6 years of the ice/ocean simulation (1986, 1990, and 1991) discussed in Secs. 4.1 and 4.2. These years were chosen to represent the early version of NOGAPS (1986) and the more recent spectral version (1990 and 1991). The upper plots of Figs. 12–14 show the weighted forcing terms for the Beaufort region computed using Eqs. 5–8. The lower plot in each figure shows the sum of the four terms (total surface forcing) and the ice thickness. The first thing to be noted in the figures is the similarity between the 1990 and 1991 forcing fluxes and how different they appear from those in 1986. The magnitude of the sensible and longwave fluxes is clearly larger more often in 1990 and 1991 than in 1986. The sensible flux is more often positive (implying heating) in 1990 and 1991 than in 1986. The net solar flux does not appear to be greatly different among these three years, even though the incoming solar values were larger in 1986 than in either 1990 or 1991. For example, the average incoming solar flux in July 1986 is about 41% greater than in July 1990. However, the net solar flux, i.e., factoring in albedo and ice concentration, is only 11% greater in July 1986 than in July 1990. The ice concentration was greater in July 1986; thus, more solar heat was reflected, while more heat was absorbed in July 1990. Ice concentration could have a similar effect on sensible heat and air temperature and on latent heat and specific humidity. This comparison, however, is complicated by the winds, which are highly variable and which significantly affect sensible and latent heat transfer.

The ice thickness and total net forcing are related in the following way: when the total net forcing is negative, ice thickness increases; when positive, ice thickness decreases. The total forcing from January through April does not greatly differ in magnitude between these 3 years, even though the individual terms differ greatly. Significant differences in the total forcing do occur in late spring and summer. These plots clearly show that the solar and sensible fluxes most often work together and oppose the latent and longwave fluxes. In the cold months (January–April and October–December), the latent and longwave are usually the stronger fluxes and cause ice growth. In the warmer months (May–September), the sensible and solar fluxes are stronger and cause melting. There are exceptions to these trends, e.g., in June and July when the latent flux sometimes becomes positive and works with the solar and sensible fluxes.

Ice thickness is strongly affected by surface forcing, as seen in Figs. 12–14. But ice advection also affects ice thickness, which is not evident from these plots. In Fig. 15, these factors are

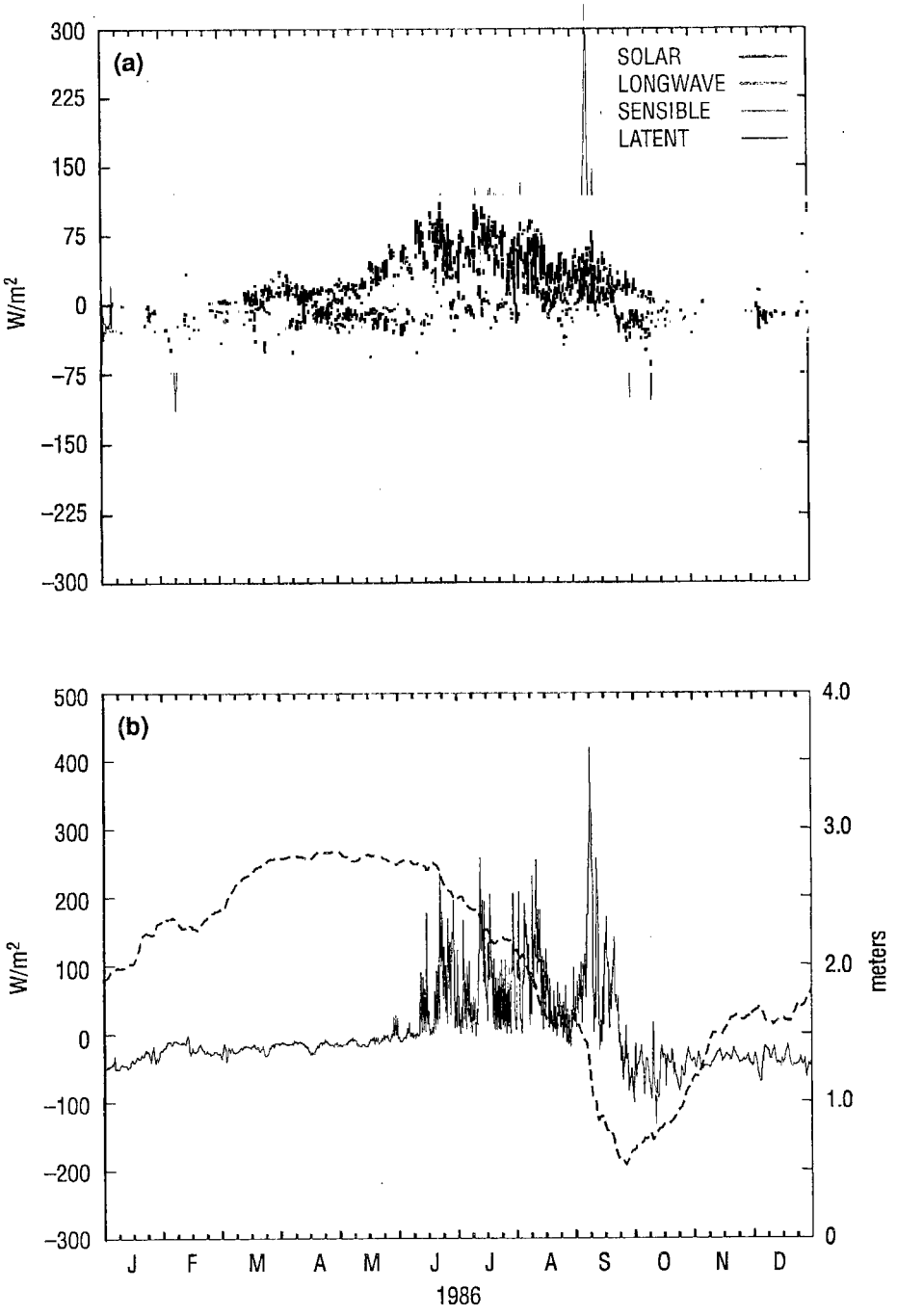

Fig. 12 — (a) Surface forcing terms from Eqs. 5–8 for 1986, Beaufort region, (b) solid line is the sum of the four forcing terms shown in (a); dotted line is the areal-averaged ice thickness in meters for the Beaufort region

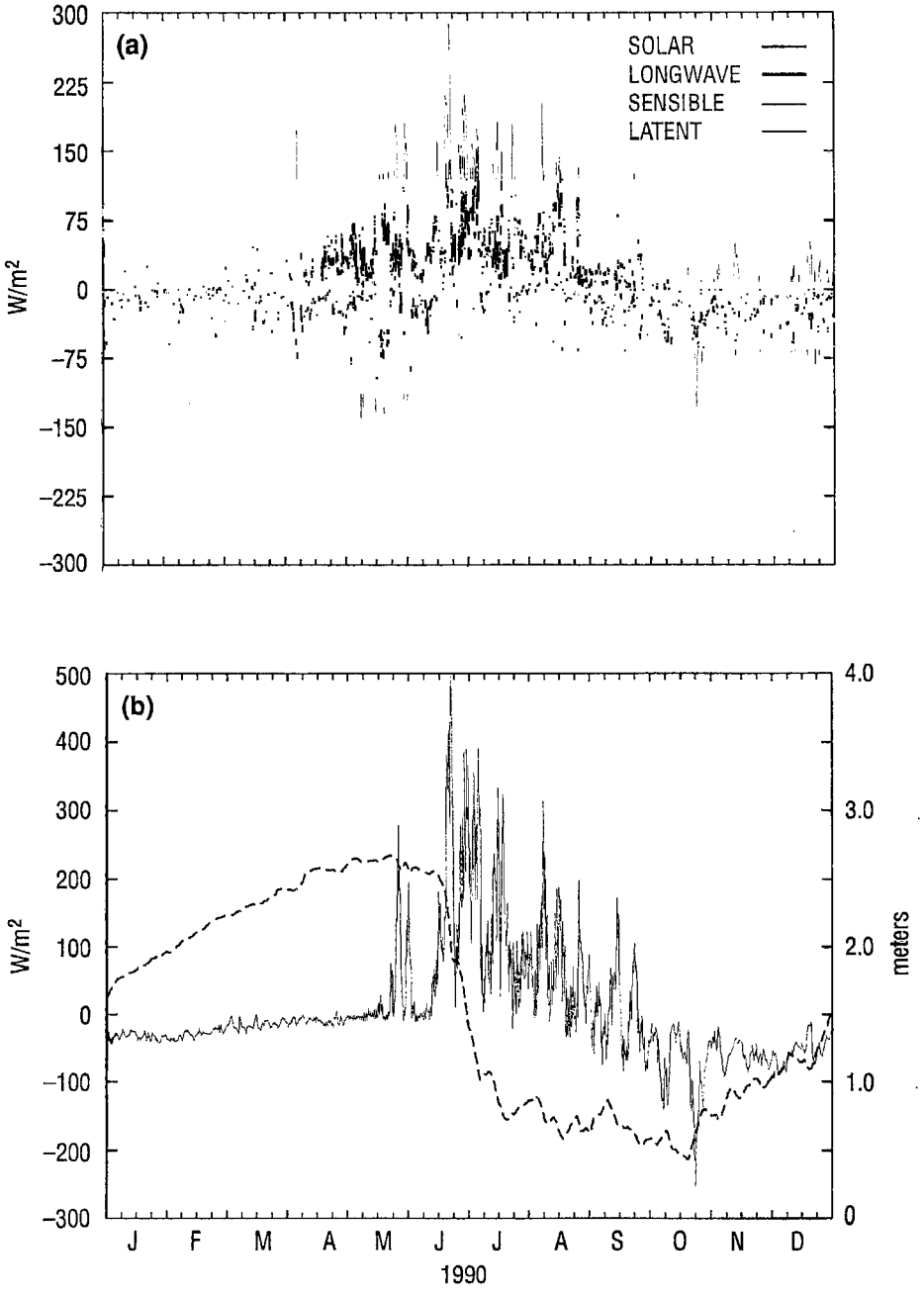

Fig. 13 — (a) Surface forcing terms from Eqs. 5–8 for 1990, Beaufort region, (b) solid line is the sum of the four forcing terms shown in (a); dotted line is the areal-averaged ice thickness in meters for the Beaufort region

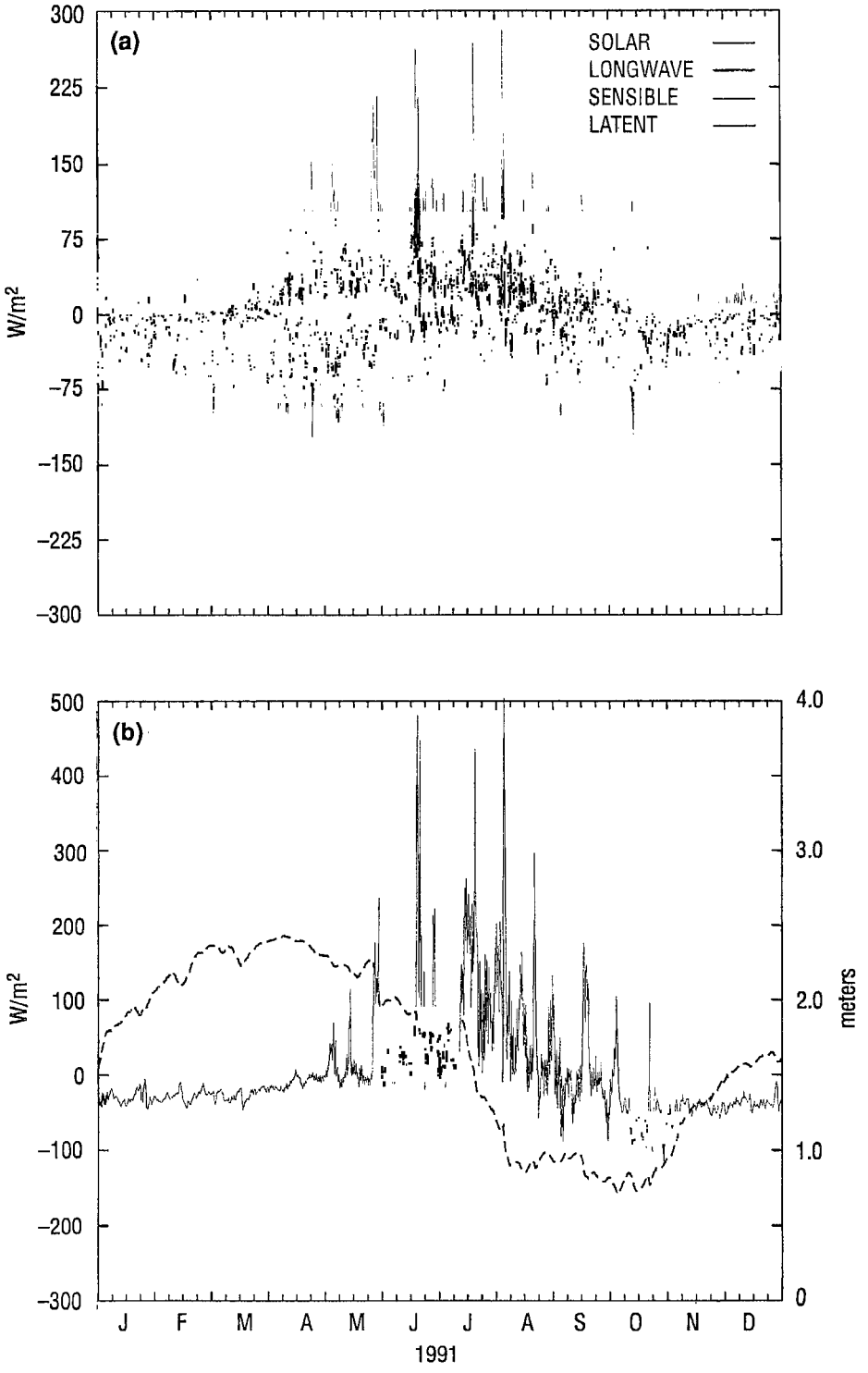

Fig. 14 — (a) Surface forcing terms from Eqs. 5–8 for 1991, Beaufort region, (b) solid line is the sum of the four forcing terms shown in (a); dotted line is the areal-averaged ice thickness in meters for the Beaufort region

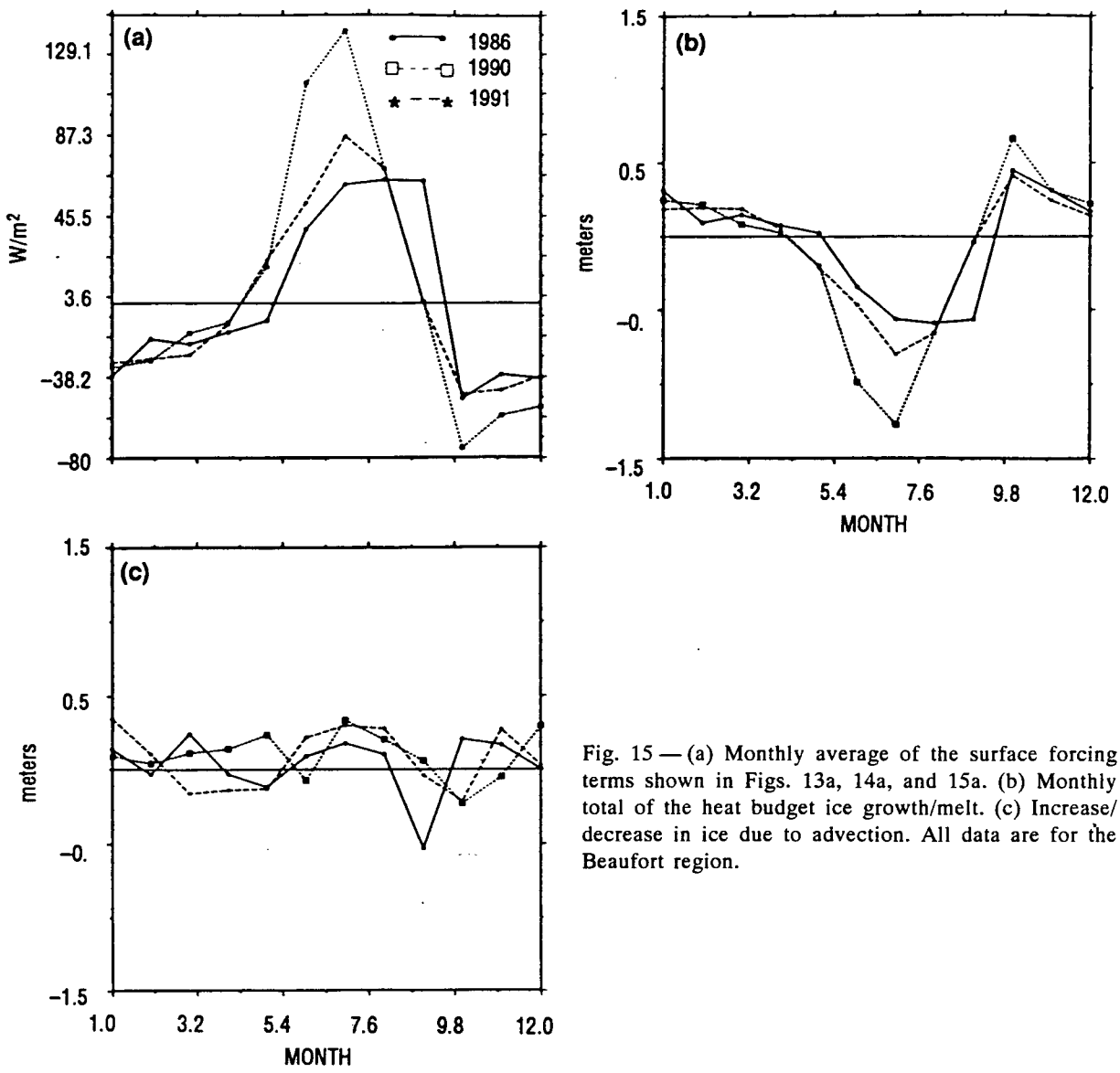

Fig. 15 — (a) Monthly average of the surface forcing terms shown in Figs. 13a, 14a, and 15a. (b) Monthly total of the heat budget ice growth/melt. (c) Increase/decrease in ice due to advection. All data are for the Beaufort region.

more clearly defined. Figure 15a shows the monthly averaged total surface forcing for each year (Figs. 12–14), Fig. 15b is the net ice growth/melt for each month, and Fig. 15c shows the amount of ice advected into or out of the region each month. It should be noted that Fig. 15b depicts the equivalent ice growth/melt due to the net heat transfer within the region. This may differ from the actual ice thickness change, particularly during late summer when there are large open-water areas where the heat transfer is not sufficient to create ice, or there is no ice present to melt. Comparing Fig. 15a and 15b, there is clearly a strong negative correlation between the total surface forcing and ice growth/melt. The oceanic heat flux (Fig. 11) is not included in Fig. 15a but is included in determining the monthly growth/melt of Fig. 15b. This heat source plays a minor role in this region in the ice growth/melt during all seasons except fall (November and December). As mentioned earlier, the total forcing does not differ greatly between the 3 years during January through April. Further, the computed growth during these months is not greatly different. Large differences occur between the years in June and July, with the strongest heating and, thus, strongest melt occurring in 1990. Examining the monthly average forcing for each of the forcing terms during these months shows that the dominant factor in the increase of total heat flux in 1990 is the sensible heat flux. Sensible heat flux is the most variable of the heat fluxes both monthly and annually.

The amount of ice advected into or out of the region during each month is shown in Fig. 15c. Advection more often brings ice into the Beaufort during these years, then removes it from the region. Comparing Fig. 15b and 15c shows that ice growth is greater in magnitude than ice advection for 7 to 9 months of each year. Advection and growth oppose each other 5 to 7 months of each year. Advection is an important component of ice thickness change, and in some regions may be as much or more important than ice growth (i.e., Greenland Sea).

5.0 SENSITIVITY STUDIES WITH CLIMATOLOGY

A further sensitivity study of the ice-ocean model response to atmospheric forcing was made by comparing model results driven by standard climatological mean forcing fields versus NOGAPS daily forcing. Three simulations were performed with climatological forcing data. The first simulation (C1) uses all climatological forcing, the second (C2) substitutes NOGAPS solar fluxes for the climatological solar fluxes, and the third (C3) substitutes NOGAPS winds for climatological winds. Each simulation is restarted from the 6-year spin-up from which the 6-year NOGAPS simulation was started. Solar fluxes and winds were chosen for these tests as their values deviated most drastically from the climatology. Each simulation is run for 1 year and then compared to each other and to the first year (1986) of the 1986–1991 6-year simulation.

The air temperature and air pressure fields used in the climatological simulations are monthly averages derived from the National Center of Atmospheric Research sea-level pressure data sets from the years 1952 through 1988. A cubic spline was used to interpolate from monthly to daily data. It was assumed that monthly data were accurate at midmonth and that each month had 30 days. The daily data were further interpolated (linearly) to the model time step (2 hours). The forcing fields—solar radiation, longwave radiation, and sensible and latent heat fluxes—are computed from the equations of Parkinson and Washington (1979). The clear-sky solar radiation Q_o is determined from the following empirical equation for global radiation under clear skies (Zillman 1972).

$$Q_o = (S \cos^2 Z) \,/\{(\cos Z + 2.7)e \times 10^{-5} + 1.085 \cos Z + 0.1\} \tag{11}$$

S is the solar constant (1353 W/m^{-2}), Z is the solar zenith angle, and e is the vapor pressure in pascals. A cloud-cover factor, c, is applied to the clear-sky solar radiation to yield the incoming solar radiation, Q

$$Q = Q_o \,(1 - 0.6c^3). \tag{12}$$

The cloud factor is 0.5 from December through March, 0.55 in April, 0.7 in May and October, 0.75 in June and July, 0.80 in August and September, and 0.6 in November. A daily average solar flux is obtained by computing Q_o at 2-hour intervals, multiplying by the time length, summing for the day, and dividing by the number of seconds in a day.

Incoming longwave radiation for clear skies F_{Lo} is computed using

$$F_{Lo} = \sigma T_a^4 \,[1 - 0.261 \exp(-7.77 \times 10^{-4} (273 - T_a)^2)]. \tag{13}$$

The Stefan-Boltzmann constant σ is 5.67×10^{-8} W/m^{-2}K^{-4}. The air temperature T_a is the climatological temperature. The same cloud factor used for solar radiation is used for longwave. The factor is applied as follows:

$$F_L = F_{Lo} \,(1 + cn), \tag{14}$$

where n is an empirical factor set at 0.275 (Parkinson and Washington 1979). The specific humidity at 10-m q_a is derived from the specific humidity at the surface q_s by assuming a relative humidity of 90%.

The climatological air temperatures, wind speed, and incoming solar fluxes for the Beaufort are shown in Fig. 16 along with the same quantities from the NOGAPS 1986 data. The climatological fields are smoothly varying compared to the NOGAPS data. Climatological wind speeds (Fig. 16a) are much smaller (<4 m/s) than the NOGAPS wind speeds. To partly compensate for the very weak climatological winds, a larger wind drag coefficient ($C_d = 2.4 \times 10^{-3}$) was used, and the wind stress was increased by a factor of 3 in the model simulation (Parkinson and Washington 1979). Although climatological air temperature and the NOGAPS data show similar seasonal trends (Fig. 16b), warmer temperatures are found in the February through April NOGAPS data. Solar radiation values are shown in Fig. 16c. The diurnal cycle, apparent in the NOGAPS data, is absent in the climatological data. The NOGAPS values are on average smaller than the climatological values, implying a greater cloud cover in the 1986 NOGAPS data. Although both data sets incorporate a cloud cover in the calculation of solar radiation, the climatological data uses a spatially invariant cloud cover that varies only monthly in time.

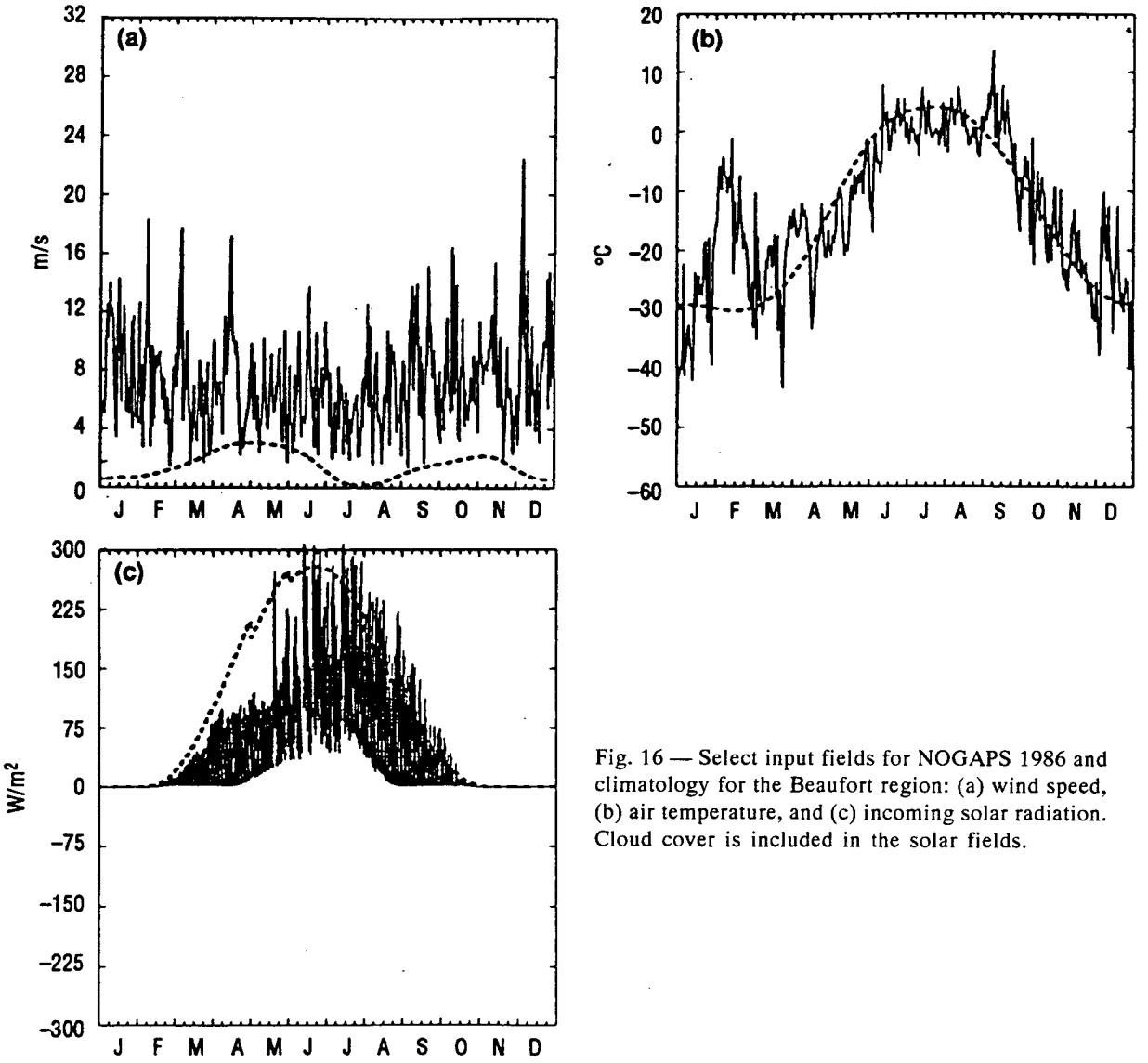

Fig. 16 — Select input fields for NOGAPS 1986 and climatology for the Beaufort region: (a) wind speed, (b) air temperature, and (c) incoming solar radiation. Cloud cover is included in the solar fields.

5.1 Test Results

Ice thickness values for the Beaufort region from a 1-year simulation for each climatological sensitivity study, and for the 1986 NOGAPS case, are shown in Fig. 17. The weighted forcing terms (Eqs. 5–8) for the climatological tests are plotted in Fig. 18. The weighted latent term is not plotted since it is usually very small. Ice thickness in test C1 (Fig. 17) thins to nearly zero in the summer. Ice begins to grow back in late October. The winds from January through March keep about 2 to 3% of the region open as leads. In April and May the winds strengthen and change direction; winds are strong enough to push the ice edge toward the pack ice, which further increases the percentage of open water/leads. At this time the magnitude of the solar forcing increases (Fig. 18a). More open water reduces the albedo of the area, so more solar heating occurs. The solar term in case C1 is 3 to 5 times greater than in the NOGAPS case. Also, the winds continue to move ice out of the area. The result is a rapid decrease in ice thickness from April to June. The other forcing fields during this time encourage cooling and ice growth (Fig. 18b and 18c), but are small relative to the solar warming and ice advection.

A small amount of ice is maintained in the northern part of the Beaufort region from June through August by ice drift. The melt rates shown in Table 5 indicate enough heat to keep the area ice-free. Most of the ice melt indicated in Table 5 during these months is actually heat absorbed by the ocean. The temperature of the first level of the ocean rises by about 6°C during these summer months.

Ice growth commences in September (Table 5), but ice thickness increases do not occur until mid-October. The heat stored in the ocean must be removed before ice growth can be maintained. This heat loss is indicated by the large negative values in the sensible and longwave terms in the fall (Fig. 18b and 18c).

In case C2, the solar fluxes from NOGAPS (1986) are substituted for the climatological fluxes. All other quantities remain the same as in case C1. The trend in the pattern of ice growth/decay in C2 is similar to that found in C1. However, starting in May, the thicknesses begin to diverge. Ice is about 0.5 m thicker in C2 than in C1 from May to December. The solar flux used in C2 (Fig. 18a) contains the diurnal variability found in the NOGAPS calculation. A "mean" curve drawn through the C2 solar flux will show consistently weaker values than those found in C1. A maximum deviation in the solar fluxes is found in the May–June time frame, causing a substantial reduction in the amount of ice melt during this time. The sensible and longwave terms, both weak cooling terms, are generally smaller in C2 than in C1.

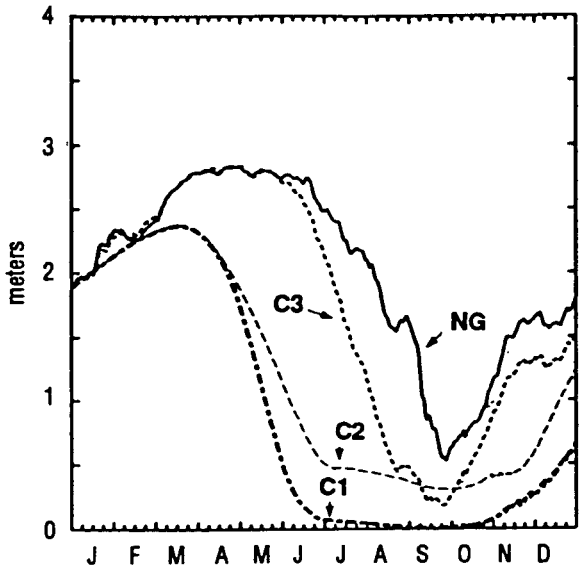

Fig. 17 — Ice thickness for the three climatological test cases and model runs with NOGAPS 1986 data for the Beaufort region.

In case C3, the NOGAPS (1986) winds and drag coefficient replace the climatological winds. Ice thickness increases by approximately 1.0 m from January through April. The vertical growth accounts for about 75% (0.74 m) of this increase. Ice thickness increases significantly in March due to advection. The NOGAPS 1986 March winds in the Beaufort cause a significant build-up of ice along the Canadian coast.

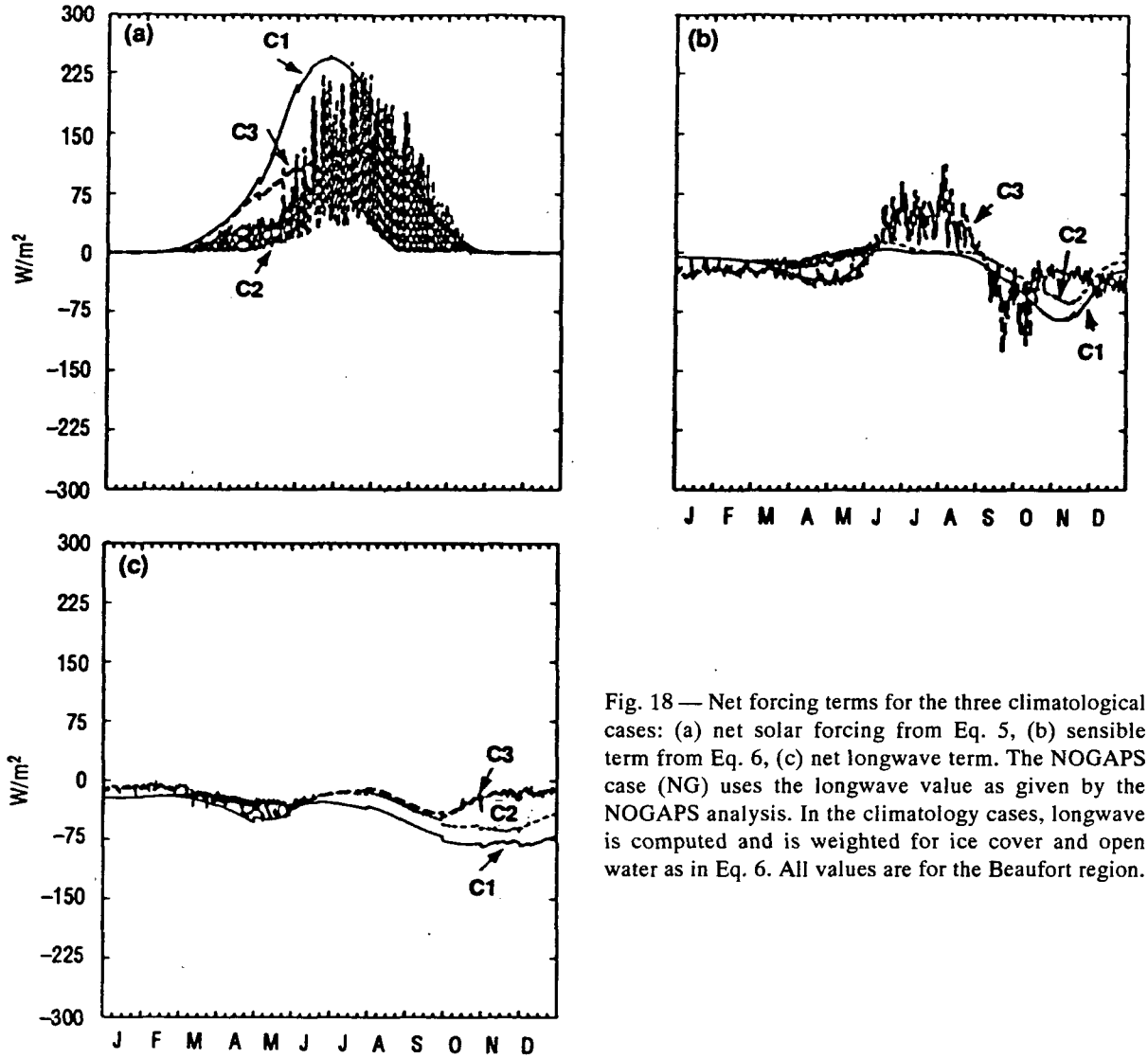

Fig. 18 — Net forcing terms for the three climatological cases: (a) net solar forcing from Eq. 5, (b) sensible term from Eq. 6, (c) net longwave term. The NOGAPS case (NG) uses the longwave value as given by the NOGAPS analysis. In the climatology cases, longwave is computed and is weighted for ice cover and open water as in Eq. 6. All values are for the Beaufort region.

Table 5 — Monthly Vertical Ice Growth from Heat Budget Calculations for the Beaufort Region

	Case C1	Case C2	Case C3	Case NG
Jan	0.187	0.187	0.284	0.313
Feb	0.195	0.199	0.243	0.094
Mar	0.168	0.185	0.150	0.148
Apr	0.077	0.146	0.062	0.077
May	−0.593	−0.008	−0.077	0.025
Jun	−1.726	−0.666	−0.860	−0.342
Jul	−1.630	−0.921	−1.262	−0.559
Aug	−0.811	−0.583	−1.050	−0.587
Sep	0.216	−0.072	0.276	−0.564
Oct	1.119	0.746	0.699	0.448
Nov	0.832	0.269	0.331	0.310
Dec	0.395	0.468	0.169	0.168

The NOGAPS winds have a significant effect on the solar, sensible, and latent heat fluxes in the summer (June–August), as seen in Fig. 18. When compared to C1, the solar and longwave fluxes have decreased in magnitude, while the sensible and latent (not shown) fluxes have increased. The greater ice concentrations keep the solar heating down, while the stronger wind increases the heat exchange of sensible and latent heat. The pattern of ice thickness increase/decrease in C3 resembles that of the NOGAPS case (NG) from January through May, indicating that the effects of wind forcing plays a dominant role during this time. From June through August, more ice is melted in the C3 case than in the NG case due to the effects of the strong climatological solar fluxes.

In summary, weak, slowly varying winds and strong solar forcing, as in case C1, yield moderate winter ice growth and rapid summer ice melt. Weak, slowly varying winds and weak solar forcing, as in C2, yield a reduction in the amount of late spring or early summer ice melt in the Beaufort compared to C1. With strong, highly variable winds that advect ice into the region in winter, the case C3 ice thickness is much greater in the winter than the case C1 ice thickness. Ice thickness decreases in summer in C3 due to the combined effects of solar and sensible heating. The ice thickness curve derived by using NOGAPS forcing (case NG) is generally thicker than the climatology cases, but shows many similarities to the C3 curve, implying that wind forcing is a dominant effect in the 1986 ice-ocean model results.

6.0 SUMMARY AND CONCLUSIONS

This study demonstrates that there is considerable variability on the interannual and seasonal time scales in the NOGAPS forcing data. The ice-ocean model shows a strong response to this variability; therefore, accurate atmospheric forcing is essential to accurate forecast modeling of the Arctic. Solar and sensible fluxes are the strongest atmospheric forcing fields and often work together to oppose the latent and longwave fluxes, resulting in summer ice melt and ocean warming. In winter (January–April), the combination of latent and longwave fluxes is stronger than and opposite to sensible heat flux, and results in cooling and ice growth. This situation usually exists in the fall (October–December) as well. The exception occurred in the fall of 1986 when the sensible heat flux removed heat from the system, resulting in more rapid cooling and ice growth.

It was also shown that winds have a strong effect on ice thickness and concentration. Winds are directly used in calculating the sensible and latent heat fluxes and affect the heat balance. Winds can also advect ice into and out of a region. By altering the percent of open water/ice cover, the winds affect the rate of heat exchange between the atmosphere and ice/ocean. In some cases, advection accounted for more than half of the change in ice thickness.

The simulations with climatological forcing reinforced the conclusion that solar heating and winds are strong factors in determining ice thickness and ice concentration. Estimates of cloud cover used in most climate studies created much stronger solar heating than the NOGAPS model and results in greater ice melt. A measure for cloud cover more accurate than that provided by climatological estimates is necessary for ice prediction. In addition, an accurate measure of the wind and its variability is necessary to determine the ice cover versus open water, which in turn is necessary for determining the exchange of heat fluxes that result in the growth/decay of sea ice.

7.0 ACKNOWLEDGMENTS

This project was funded by the Office of Naval Research, Technology Directorate, through the Naval Ocean Modeling and Prediction Program (program element 0602435N). Mr. Robert Peloquin was program manager.

8.0 REFERENCES

Bourke, R. H. and R. P. Garrett, "Sea Ice Distributions in the Arctic Ocean," *Cold Reg. Sci. Technol.* **13**, 259–280 (1987).

Colony, R. L. and I. Rigor, "Arctic Ocean Buoy Program Data Report for 1 January 1986–31 December 1986," Tech. Memo. APL-UW TM6-89, 139 p., Applied Physics Laboratory, University of Washington, Seattle, WA, 1989.

Colony, R. L. and I. Rigor, "Arctic Ocean Buoy Program Data Report for 1 January 1987–31 December 1987," Tech. Memo. APL-UW TM7-91, 152 p., Applied Physics Laboratory, University of Washington, Seattle, WA, 1991a.

Colony, R. L. and I. Rigor, "Arctic Ocean Buoy Program Data Report for 1 January 1988–31 December 1988," Tech. Memo. APL-UW TM8-91, 181 p., Applied Physics Laboratory, University of Washington, Seattle, WA, 1991b.

Colony, R. L. and I. Rigor, "Arctic Ocean Buoy Program Data Report for 1 January 1989–31 December 1989," Tech. Memo. APL-UW TM9-91, 158 p., Applied Physics Laboratory, University of Washington, Seattle, WA, 1991c.

Colony, R. L. and I. Rigor, "Arctic Ocean Buoy Program Data Report for 1 January 1990–31 December 1990," Tech. Memo. APL-UW TM10-91, 142 p., Applied Physics Laboratory, University of Washington, Seattle, WA, 1991d.

Cox, M., "A Primitive Equation, 3-Dimensional Model of the Ocean," GFDL Ocean Group Tech. Rep., 1141 p., Geophysical Fluid Dynamics Laboratory, Princeton, NJ, 1984.

Hibler, W. D. III, "A Dynamic Thermodynamic Sea Ice Model," *J. Phys. Oceanogr.* **9**, 815–864 (1979).

Hibler, W. D. III and K. Bryan, "A Diagnostic Ice-Ocean Model," *J. Phys. Oceanogr.* **17**, 987–1015 (1987).

Hogan, T. F. and T. E. Rosmond, "The Description of Navy Operational Global Atmospheric Prediction System's Spectral Forecast Model," *Mon. Wea. Rev.* **119**, 1786–1815 (1991).

Hogan T. F., T. E. Rosmond, and R. Gelaro, "The Description of the Navy Operational Global Atmospheric Prediction System's Forecast Model," NOARL Report 13, Naval Research Laboratory, Stennis Space Center, MS, 1990.

Levitus, S., "Climatology Atlas of the World Ocean," NOAA Prof. Pap., **13**, 173 p. (1982).

Naval Oceanographic Office, "Data Base Documentation for Digital Bathymetric Data Base Confidential (DBDBC)," Doc. OAML-DBD-17A, Naval Oceanographic Office, Stennis Space Center, MS, 1987.

Navy/NOAA Joint Ice Center, "Eastern-Western Arctic Sea Ice Analyses 1986," Naval Polar Oceanography Center, Washington, DC, 1986.

Navy/NOAA Joint Ice Center, "Eastern-Western Arctic Sea Ice Analyses 1987," Naval Polar Oceanography Center, Washington, DC, 1987.

Navy/NOAA Joint Ice Center, "Eastern-Western Arctic Sea Ice Analyses 1988," Naval Polar Oceanography Center, Washington, DC, 1988.

Navy/NOAA Joint Ice Center, "Eastern-Western Arctic Sea Ice Analyses 1989," Naval Polar Oceanography Center, Washington, DC, 1989.

Navy/NOAA Joint Ice Center, "Eastern-Western Arctic Sea Ice Analyses 1990," Naval Polar Oceanography Center, Washington, DC, 1990.

Navy/NOAA Joint Ice Center, "Eastern-Western Arctic Sea Ice Analyses 1991," Naval Polar Oceanography Center, Washington, DC, 1991.

Parkinson, C. L. and W. M. Washington, "A Large-Scale Numerical Model of Sea Ice," *J. Geophys. Res.*, **84**, 311-337 (1979).

Preller, R. H. and P. G. Posey, "The Polar Ice Prediction System—A Sea Ice Forecasting System," NORDA Report 212, Naval Research Laboratory, Stennis Space Center, MS, 1989.

Riedlinger, S. H. and R. H. Preller, "The Development of a Coupled Ice-Ocean Model for Forecasting Ice Conditions in the Arctic," *J. Geophys. Res.* **96**, 16955–16977 (1991).

Sarmiento, J. L. and K. Bryan, "An Ocean Transport Model for the North Atlantic," *J. Geophys. Res.* **87**, 395–408 (1982).

Walsh, J. E., W. D. Hibler III, and B. Ross, "Numerical Simulation of Northern Hemisphere Sea Ice Variability, 1951–1980," *J. Geophys. Res.* **90**, 4847–4856 (1985).

Zillman, J. W., "A Study of Some Aspects of the Radiation and Heat Budgets of the Southern Hemisphere Oceans," *Meteorol. Stud.* **26**, 562 p., Bureau of Meteorology, Department of the Interior, Canberra, Australia (1972).